Mechanical Engineering Advances 2026, 4(1), 3942.
doi: https://doi.org/10.59400/mea3942

Article

Numerical investigation of induction hardening of stationary cylindrical steel pins with convective quenching

Mohammad Yaghoub Abdollahzadeh Jamalabadi

Department of Marine Engineering, Chabahar Maritime University, Chabahar 99717-56499, Iran; my.abdollahzadeh@cmu.ac.ir

CITATION

Jamalabadi MYA. Numerical investigation of induction hardening of stationary cylindrical steel pins with convective quenching. Mechanical Engineering Advances. 2026; 4(1): 3942. https://doi.org/10.59400/mea3942

ARTICLE INFO

Received: 2 November 2025
Revised: 20 December 2025
Accepted: 24 December 2025
Available online: 15 January 2026

Abstract: This paper presents a comprehensive, fully-coupled Multi-physics finite element model for simulating the induction hardening process of stationary cylindrical steel pins, including subsequent convective cooling. The model integrates three interacting physics domains—electromagnetic induction, transient heat transfer, and metallurgical phase transformations—within an efficient two-dimensional axisymmetric formulation. Temperature-dependent material properties for all steel phases (ferrite, pearlite, austenite, martensite) and the surrounding air are implemented, and the formulation accounts for latent heat effects during phase changes. The framework employs a segregated solver approach, ensuring robust convergence between the strongly coupled electromagnetic, thermal, and phase transformation modules. The stationary configuration simplifies the computational approach while retaining high fidelity for industrial applications. The simulation predicts critical process outcomes such as transient temperature distributions, phase evolution, and the resulting spatially-graded hardness profile. It further evaluates the resultant residual stress distribution, providing insight into potential distortion and component performance. Furthermore, it serves as a predictive tool for optimizing key operational parameters, including induction coil current frequency and magnitude, heating time, and forced convective cooling intensity. Model predictions for case depth versus applied power show strong agreement with experimental measurements, validating the framework. The validated model demonstrates its utility as a virtual design platform, reducing the need for costly experimental trials. This integrated model provides a complete and practical computational framework for designing, analyzing, and optimizing stationary induction hardening processes to achieve targeted hardness depths, improve energy efficiency, and ensure consistent product quality in manufacturing.

Keywords: induction hardening; Multiphysics modeling; phase transformation; axisymmetric formulation; convective cooling; finite element analysis; process optimization

1. Introduction

Induction hardening is a widely used surface treatment process that enhances wear resistance and fatigue strength of steel components through localized heating and rapid quenching. In many industrial applications, workpieces remain stationary while the induction coil provides controlled heating, followed by a quenching phase using convective cooling or controlled air flow.

The plots in **Figure 1** provide a comprehensive visual and schematic overview of the induction hardening process, which is used to selectively harden the surface of metal components such as gears. **Figure 1a** shows a photograph of an actual

induction hardening setup, offering a real-world view of the equipment. **Figure 1b** presents a schematic diagram illustrating key elements, including the induction coil, magnetic field lines, the workpiece (a gear), and the flow of current. In **Figure 1c**, a cross-sectional view highlights the structural relationship between the induction coil, the air gap, and the workpiece, clearly distinguishing the hardened surface layer (case) from the softer, unhardened core, and indicating the case depth. Finally, **Figure 1d** displays a temperature-time profile graph, depicting the thermal cycle involved: rapid heating to above the austenitizing temperature (Au temperature of 723 °C), a brief holding period, and subsequent quenching. The graph axes plot time in seconds against temperature in °C, effectively capturing the critical heating and cooling stages of the process.

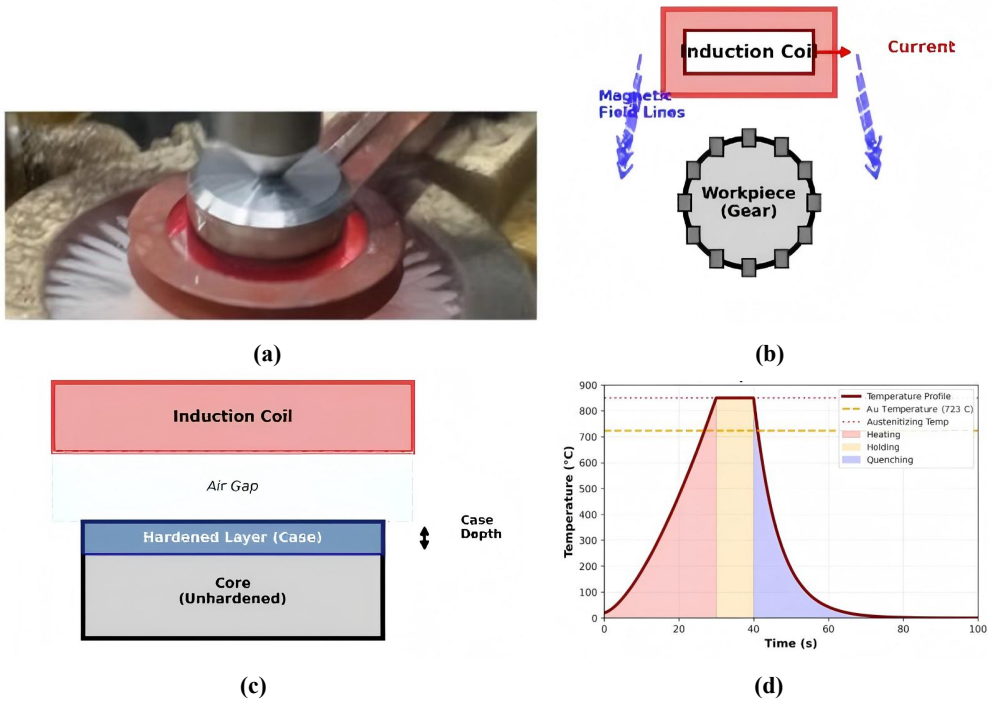

Figure 1. Induction harnessing process comprehensive overview: **(a)** actual induction hardening setup; **(b)** key elements—schematic representation; **(c)** a cross-sectional view; **(d)** temperature-time profile graph.

Recent research has advanced the understanding of induction hardening through both experimental and computational approaches. Evolutionary optimization techniques combining response surface methodology (RSM) with desirability functions have demonstrated successful industrial implementation for process parameter optimization [1]. Data-driven inverse problem formulations have emerged as powerful alternatives to traditional forward modeling, enabling determination of optimal process parameters from desired microstructural outcomes with significantly reduced computational cost [2,3].

The coupling of electromagnetic, thermal, and metallurgical physics domains has been progressively refined, with recent implementations incorporating improved convergence algorithms and validation against industrial measurements [4, 5]. Phase transformation modeling has progressed significantly through integration of

data-driven approaches with traditional continuous cooling transformation (CCT) kinetics [6,7].

Mathematical modeling approaches have been developed to predict temperature distributions, phase transformations, and resulting material properties during induction hardening processes [8,9]. Non-isothermal phase transformation kinetics, particularly the austenization behavior during heating cycles, have been characterized using Johnson-Mehl-Avrami equations for various steel grades [10]. The future of Induction Hardening technology looks promising, with continued advancements in materials science, precision engineering, and digital integration. However, the industry also faces challenges, including the need for skilled labor, the high cost of advanced materials and technologies, and the integration of new systems into existing infrastructure [11].

Based on the cited research, alternating magnetic fields significantly influence temperature evolution and phase change phenomena during metallic droplet solidification and in ferromagnetic fluid flows. Specifically, Sharifi and Amani [12] demonstrate that electromagnetic effects during the impact and solidification of a metallic alloy droplet can alter the cooling rate and final microstructure by inducing internal fluid motion, which redistributes heat within the droplet [12]. Further analysis by Amani and Sharifi [13] on droplet impact under an alternating magnetic field establishes scaling laws and regime maps, showing that the AC field can control the solidification front and the spatiotemporal temperature profile by modifying convective heat transfer, thereby dictating transitions between spreading, splashing, and solidification regimes [13]. Complementing these findings, Sharifi [14] reveals that magnetic fields can profoundly modify heat transfer in turbulent ferromagnetic flows, such as over a backward-facing step, by damping turbulence and restructuring flow vortices, which directly affects the thermal boundary layer and overall temperature distribution [14]. Collectively, these studies confirm that applied AC magnetic fields are a powerful tool for actively managing thermal transport and phase-change dynamics in metallic systems.

The modeling of induction hardening is built upon a rich foundation of induction heating principles and steel metallurgy. Rudnev et al. [15] provide a comprehensive industrial handbook that details the electromagnetic, thermal, and practical aspects of induction heating, serving as a crucial reference for defining process parameters and boundary conditions. The fundamental physics of coupled phenomena in this process was mathematically formalized in early works such as that of Hömberg [16], who developed a model integrating thermal and mechanical effects, establishing a basis for the fully coupled Multiphysics approaches used today. From a historical perspective, Mühlbauer [17] documents the evolution of induction technology, highlighting the transition from empirical methods to model-based design. Validating such models, especially for critical outputs like residual stress, is essential; Coupard et al. [18] directly compare simulated and measured residual stresses in inductively hardened steel, demonstrating the capability and limitations of contemporary simulation frameworks in predicting mechanical outcomes. Advances in process control are explored by Hirao and Ogi [19], who investigate in-situ monitoring techniques using electromagnetic acoustic transduction, representing the shift towards smart, sensor-integrated manufacturing systems. At the core of any microstructure prediction

model lies the physical metallurgy of steels. The authoritative text by Bhadeshia and Honeycombe [20] provides the essential theory and data on phase transformations, microstructure-property relationships, and transformation kinetics, including the foundational Koistinen-Marburger equation [21] for martensitic transformation, which remains a standard in computational models. Applying these principles to complex geometries, Pinheiro et al. [22] demonstrate a Multiphysics simulation for gear teeth, incorporating magnetic flux concentrators, thereby extending axisymmetric models to more intricate, real-world components. The numerical methodology for solving coupled magneto-thermo-elastic problems is further elaborated in works like that of Toros and Altinel [23], who analyze functionally graded materials under coupled fields, illustrating solution strategies for similar multi-physics couplings. Finally, the comprehensive doctoral work of Sjöström [24] on modeling phase transformations under concurrent stress, strain, and temperature fields provides a critical theoretical framework for understanding transformation-induced plasticity (TRIP) and the development of internal stresses, which are key to predicting final component distortion and performance.

To improve the accuracy of the study, a robust and comprehensive multi-physics model by employing coupled 2D axisymmetric finite element (FE) simulations with iterative time-stepping should be used to solve the intricate interplay of electromagnetics, heat transfer, and phase changes [25]. For instance, the Finite Difference Method (FDM) offers a straightforward discretization approach often prized for its computational efficiency in structured domains, as adapted for stress analysis in composites by Wang et al. [26]. Alternatively, the Bézier Multi-Step Method utilizes Bézier curves for spatial discretization, providing high-order accuracy and smooth stress solutions, as demonstrated by Kabir and Aghdam for analyzing notched nanocomposite plates [25]. Furthermore, advanced coupling strategies like coupled FE meshes, which allow different mesh regimes to interact at interfaces, provide a sophisticated means to handle multi-domain physics, such as fluid-structure interaction explored by Jamalabadi [27]. These alternatives highlight the rich toolbox available for multi-physics simulation, where the selection of method often depends on the specific demands of geometry, material properties, and computational resources.

The aim of the current investigation is to integrate three coupled physics domains for stationary induction hardening: electromagnetics, heat transfer, and metallurgical phase transformations. This work provides a comprehensive framework for stationary hardening processes by incorporating:

- Complete 2D axisymmetric formulation for computational efficiency;
- Temperature-dependent electromagnetic and thermal properties;
- Detailed phase transformation kinetics with latent heat effects;
- Convective cooling boundary conditions for quenching simulation.

2. Mathematical model

Table 1 shows the simulation parameters. The geometry is axisymmetric, allowing simulation of only half the domain in two dimensions. The cylindrical pin remains stationary within the induction coil during the heating phase, followed by a cooling

phase with convective heat transfer. More property data is in **Appendix A**.

Table 1. Primary simulation parameters.

Parameter	Value
Pin radius	0.02954 m
Pin length	0.01 m
Coil inner radius	0.06111 m
Coil length	0.01905 m
Coil frequency	120–350 kHz
power	50–110 kW
Heating time	0.1–1.0 s
Cooling time	10.0 s

For the axisymmetric cylindrical pin geometry, we use cylindrical coordinates (r, z, θ) where r is the radial coordinate, z is the axial coordinate along the pin axis, and θ is the azimuthal angle. Due to symmetry, all field variables are functions of (r, z) only, with no θ dependence.

The magnetic vector potential A satisfies the diffusion equation for stationary conductors:

$$\nabla \times \left(\frac{1}{\mu}\nabla \times \mathbf{A}\right) + \sigma\left(\frac{\partial \mathbf{A}}{\partial t} - \mathbf{v} \times (\nabla \times \mathbf{A})\right) = \mathbf{J}_{\text{ext}} \tag{1}$$

where μ is the magnetic permeability (temperature dependent for steel), σ is the electrical conductivity (temperature dependent), and $\mathbf{J}_{\text{ext}}$ is the external current density in the coil windings with angular frequency of ω (2πf).

For axisymmetric geometry with azimuthal current flow, the magnetic vector potential has only a θ-component: $A = A\_\theta(r, z)$. The governing equation in 2D axisymmetric form becomes:

$$\frac{1}{r}\frac{\partial}{\partial r}\left(\frac{r}{\mu}\frac{\partial A_\theta}{\partial r}\right) + \frac{\partial}{\partial z}\left(\frac{1}{\mu}\frac{\partial A_\theta}{\partial z}\right) - \frac{A_\theta}{\mu r^2} + \sigma\left(\frac{\partial A_\theta}{\partial t} - v_z\frac{\partial A_\theta}{\partial z}\right) = J_{\theta,\text{ext}} \tag{2}$$

The induced eddy current density in the pin is:

$$J_\theta = \sigma\left(-\frac{\partial A_\theta}{\partial t} + v_z\frac{\partial A_\theta}{\partial z}\right) \tag{3}$$

The electromagnetic energy dissipated as Joule heating provides the volumetric heat source:

$$Q_{\text{ind}}(r, z, t) = \frac{J_\theta^2}{\sigma} = \sigma\left(\frac{\partial A_\theta}{\partial t} - v_z\frac{\partial A_\theta}{\partial z}\right)^2 \tag{4}$$

The temperature field T evolves according to the transient heat equation:

$$\rho C_p\left(\frac{\partial T}{\partial t} + v_z\frac{\partial T}{\partial z}\right) = \frac{1}{r}\frac{\partial}{\partial r}\left(rk\frac{\partial T}{\partial r}\right) + \frac{\partial}{\partial z}\left(k\frac{\partial T}{\partial z}\right) + Q_{\text{Joule}} + Q_{\text{phase}} \tag{5}$$

where ρ is the mass density, C_p is the specific heat capacity, k is the thermal

conductivity, Q_{Joule} is the Joule heating from eddy currents, and Q_{phase} represents latent heat sources/sinks from phase transformations. All material properties are functions of temperature and phase composition, calculated using the mixture rule.

Heat transfer at the boundaries includes convection to air and thermal radiation:

$$-k\nabla T \cdot n = h(T - T_{\infty}) + \varepsilon\sigma_{SB}(T^4 - T_{\infty}^4) \quad (6)$$

where h is the convective heat transfer coefficient, T_{∞} is the ambient temperature, ε is the emissivity, and σ_{SB} is the Stefan-Boltzmann constant. During the heating phase, h = 15 W/(m^2·K) for natural convection. During the quenching phase (t > 1 s), forced convection of water spray is applied to simulate accelerated cooling. More discussion on heat transfer is in **Appendix B**.

The metallurgical transformations in steel involve both heating and cooling phase changes. During heating, the initial microstructure (ferrite + pearlite) transforms to austenite. During quenching, the austenite transforms to various products depending on cooling rate: ferrite, pearlite, bainite, or martensite. Some of the most important metallurgical property data are in **Appendix A**.

The simulation models two types of transformations: Diffusive Transformations (Ferrite, Pearlite, Bainite) and Displacive Transformation (Martensite). Diffusive transformations are governed by TTT (Time-Temperature-Transformation) curves, while Martensite forms by a diffusion-less mechanism characterized by Martensite Start Temperature. The initial microstructure of the pin starts as 50% ferrite + 50% pearlite (typical annealed steel). The simulation calculates austenite, ferrite, pearlite, bainite, and martensite through:

1. Importing comprehensive material data (TTT curves, M_s temperatures, material properties);
2. Tracking temperature history at each point via coupled electromagnetic-thermal analysis;
3. Applying transformation kinetics:
   - Diffusive transformations: TTT curves and Johnson-Mehl-Avrami-Kolmogorov equation
   - Martensite: Koistinen-Marburger equation based on M_s
4. Enforcing mass conservation: All phase fractions sum to 1;
5. Coupling with mechanics and heat transfer: Latent heat, transformation strains, TRIP.

Austenitization during heating is modeled using a linear kinetic model:

$$dX\_\gamma/dt = (1 - X\_\gamma)/(t\_aus(T, dT/dt)) \text{ for } A_1 < T < A_3 \quad (7)$$

where X_γ is the austenite fraction, $A_1 \approx 723$ °C is the lower austenitization temperature, and $A_3 \approx 850$ °C is the upper austenitization temperature.

Material Type used here is General Steel with the steel grade of AISI 4140 and carbon content ~0.4 wt.% with a hardness of 400 VPN (Vickers hardness). Its microstructure is quenched and tempered (fine), and the austenitization temperature

is 860 °C. Upon quenching, austenite decomposes according to continuous cooling transformation (CCT) kinetics. The transformation products are modeled using the Avrami equation with temperature-dependent parameters. Martensite formation occurs when the cooling rate is sufficiently rapid, modeled using the Koistinen-Marburger equation:

$$X_M = X_{\gamma,0}[1 - \exp(-\beta(M_s - T))] \quad (8)$$

where $\beta = 0.011\ K^{-1}$, $M_s = 330$ °C is the martensite start temperature, and $X_{\gamma,0}$ is the austenite fraction at the start of quenching. It is noticeable that Koistinen–Marburger constant typically is ~0.011–0.035 $°C^{-1}$ for steels. **Figure 2** presents a schematic of the process. Based on phase strain and thermal strains, the stress field is updated in each step. More data about the stress-strain field is in **Appendix C**.

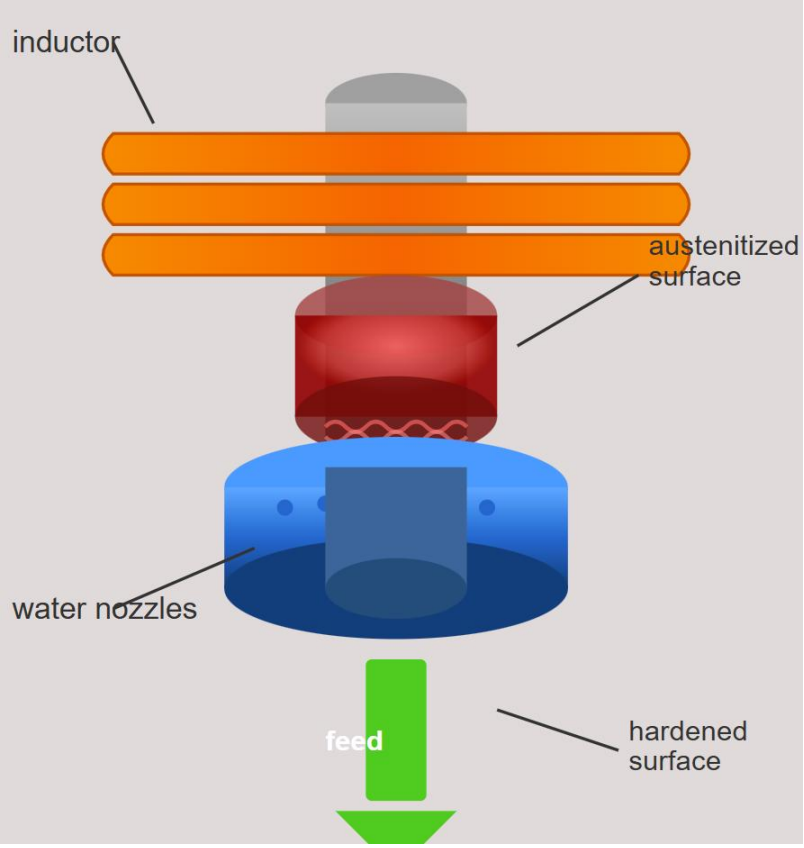

Figure 2. Schematic of the process.

The mathematical model is based on the following key assumptions that are mentioned in the introduction section to balance computational efficiency with physical accuracy:

1. **Axisymmetric 2D formulation:** The geometry of the cylindrical pin and coil is assumed to be perfectly axisymmetric. This allows the reduction of the three-dimensional problem to a two-dimensional domain in cylindrical coordinates (r, z), where all field variables are independent of the azimuthal angle θ. This simplification significantly reduces computational cost while maintaining accuracy for symmetric workpieces.
2. **Quasi-static electromagnetic approximation:** The model adopts the

magnetoquasistatic approximation, neglecting displacement currents ($\partial t \partial \mathbf{D} \approx 0$) in Maxwell's equations. This is valid for the induction hardening process, where the operating frequencies (120–350 kHz) are sufficiently low that the electromagnetic wave propagation effects are negligible compared to diffusion-dominated eddy current formation.

3. **Nonlinear magnetic permeability:** The magnetic permeability $\mu\mu$ of the steel workpiece is treated as temperature- and phase-dependent. The nonlinear B-H relationship for AISI 4140 steel is incorporated through tabulated material data, accounting for saturation effects, which is critical for accurately predicting eddy current penetration and heating power density.
4. **Velocity terms in heat equation:** The convective terms involving velocity **v** in the heat transfer equation (Equation (5)) are retained in the general form for modeling the forced convective cooling phase. It is clarified that the workpiece is stationary; therefore, **v** represents the velocity field of the quenching medium (air or liquid) in the boundary layer, not the motion of the pin itself. During natural convection in the heating phase, these terms are negligible.

3. Results and discussion

The Multiphysics model is implemented using the finite element method in a two-dimensional axisymmetric formulation. The computational domain consists of the steel pin, copper coil, and surrounding air. The finite element mesh uses quadrilateral elements with boundary layer refinement at the pin surface to resolve steep electromagnetic and thermal gradients. With a skin depth of approximately 0.3 mm at 120 kHz, the boundary layer mesh provides 6 elements within 1 mm from the surface. At 350 kHz, the skin depth is approximately 0.17 mm (vs. 0.3 mm at 120 kHz). To ensure accuracy, the mesh was refined to maintain at least 8 elements within one skin depth at the highest frequency used (350 kHz). This ensures adequate resolution of the electromagnetic and thermal gradients near the surface. The revised manuscript now includes this clarification.

The time-dependent study uses a segregated solver approach where each physics module is solved sequentially within each time step, iterating until all fields are mutually consistent. The coupling workflow follows these steps:

1. Solve electromagnetics: Compute magnetic vector potential A and eddy current density J;
2. Compute Joule heating: $Q_{Joule} = |J|^2/\sigma$;
3. Solve heat transfer: Update temperature field T;
4. Update phase fractions: Compute transformation rates and integrate;
5. Calculate transformation heats: $Q_{phase;}$
6. Update material properties: Recompute μ, σ, k based on new T and phase fractions.

The simulation provides detailed predictions of the induction hardening process for the stationary pin configuration.

Temperature distribution

The simulation shows peak surface temperatures of 950–1050 °C achieved during the heating phase. The core temperature remains significantly cooler at 600–700 °C, ensuring only surface hardening occurs. During the quenching phase with enhanced convection (h = 150 W/(m^2·K)), surface cooling rates of 150–300 °C/s are achieved, which is sufficient for martensite formation in medium-carbon steels (**Figure 3**).

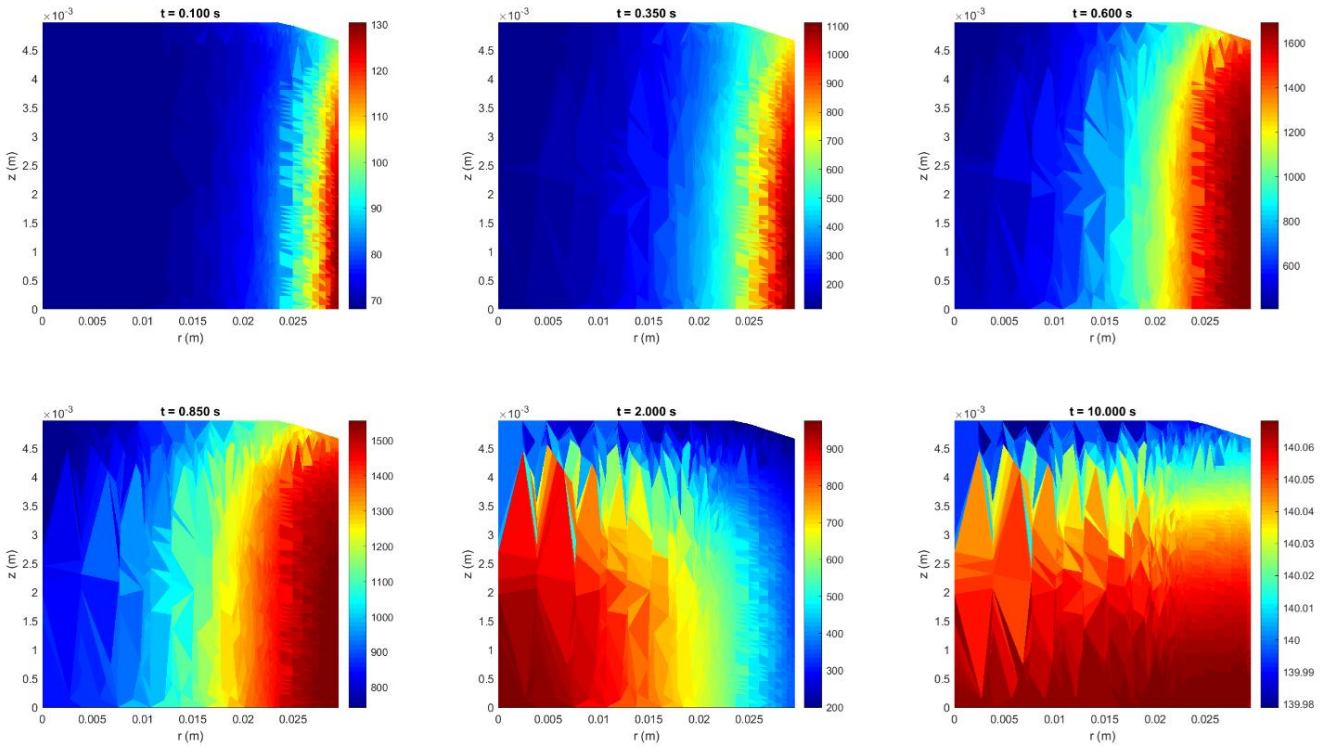

Figure 3. Temperature Distribution in Fahrenheit degrees versus time in seconds.

As shown in **Figure 4a,** the phase transformation model predicts a martensitic case depth of approximately 1.5–2.5 mm, with a transition zone of 0.3–0.5 mm thickness between the fully martensitic case and the unaffected core. The core microstructure remains largely unchanged, consisting of the original ferrite and pearlite phases. **Figure 4b** shows the residual von Mises stress at the end of the process.

Based on the provided **Figure 5**, Induction Case Depth vs Load Power (τ = 0.3–1 s, f = 350 kHz), the plot compares the relationship between applied load power and the resulting case depth from an induction hardening process, with a fixed heating time τ of 0.3 s and a frequency of 350 kHz. The blue line represents the trend predicted by numerical simulation, while the red dots indicate experimentally measured data points. The x-axis is scaled in kilowatts (kW) of load power, and the y-axis shows the case depth in mils (thousandths of an inch). This type of graph is commonly used to validate simulation models against real-world outcomes in materials processing, illustrating how increases in power generally lead to greater hardened depth until saturation or practical limits are reached.

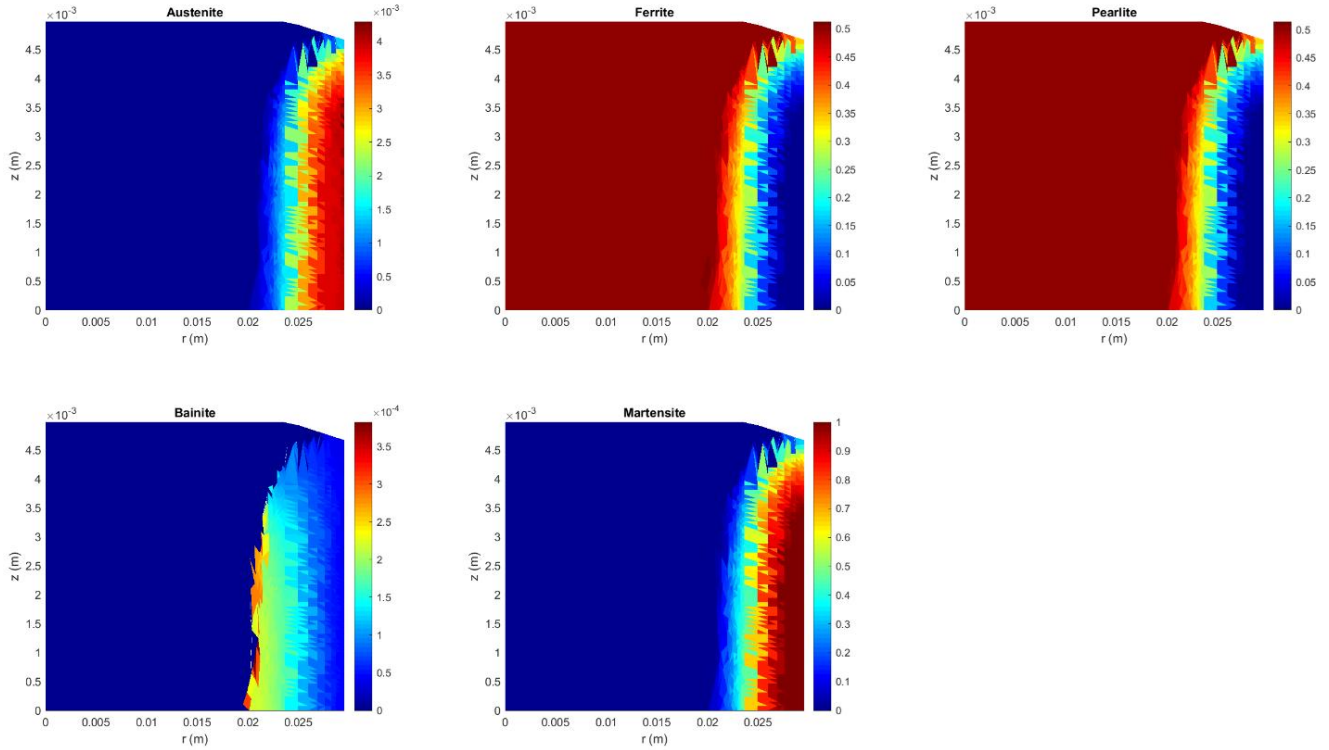

(a)

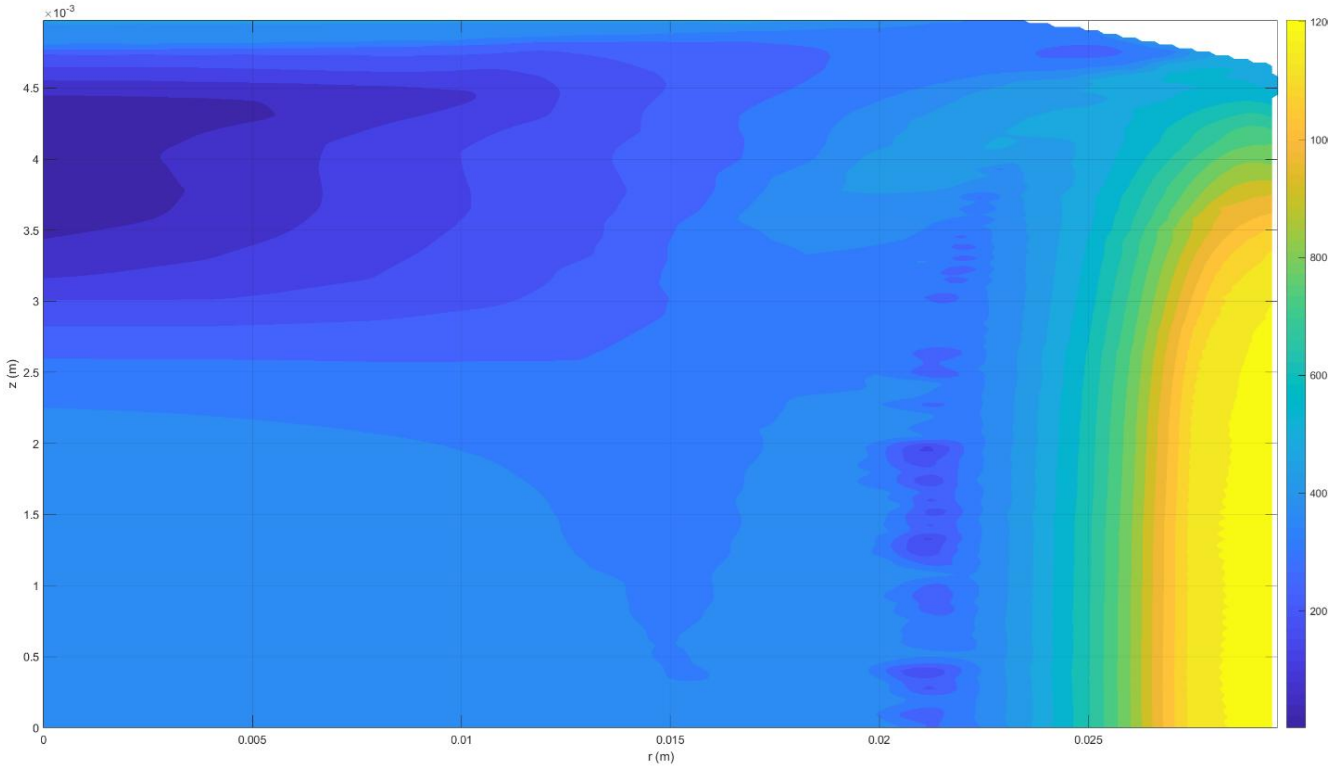

(b)

Figure 4. Microstructure Predictions at the end of the process (t = 10 s): **(a)** Phase contents; **(b)** residual stress.

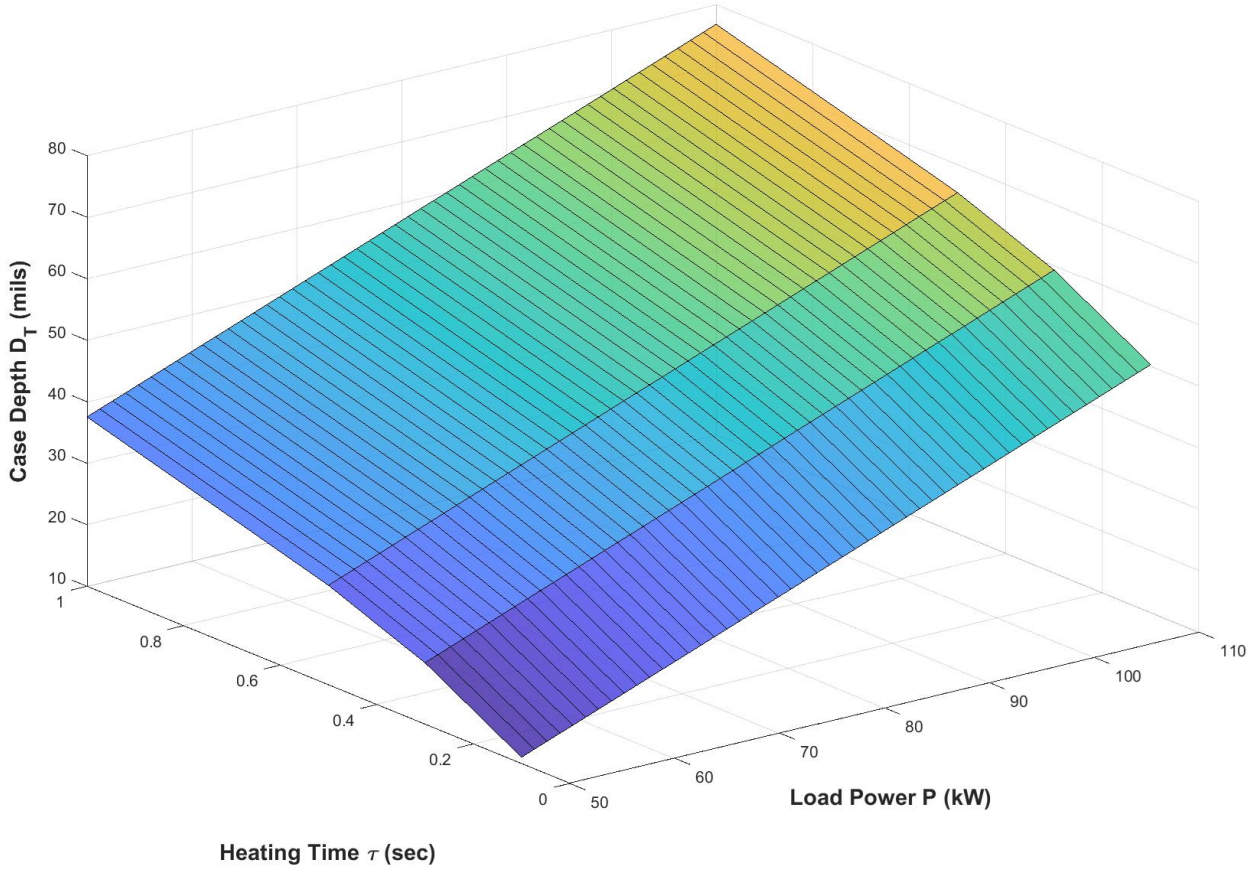

Figure 5. Effective case depth based on Microstructure predictions.

Device of Induction Systems, Inc. [28] with powerflex integration is used here. The 20-turn coil with a filling factor of 0.8 is used. Device type is a power inverter system that is equipped with a power meter, current meter, and voltage meter. Output display, displays inverter output from 0–10 V (possibly an analog or scaled output). The inverter coil (inductor) has a configuration of standard transformer tap settings.

Figure 6 is about induction case depth vs load power, which illustrates the correlation between the applied load power and the resulting hardened case depth achieved through an induction heating process, conducted under specific parameters of pulse duration τ = 0.3 s, and frequency f = 350 kHz. The graphical comparison presents a blue line depicting the trend from a numerical simulation, alongside red dots marking the actual experimental measurements. With load power (in kilowatts) on the horizontal axis and case depth (in mils) on the vertical axis, the plot serves to validate the accuracy of the computational model against empirical data. The close alignment between the simulated curve and the experimental points typically indicates a reliable model, demonstrating how increases in power input enhance penetration depth within the given processing window.

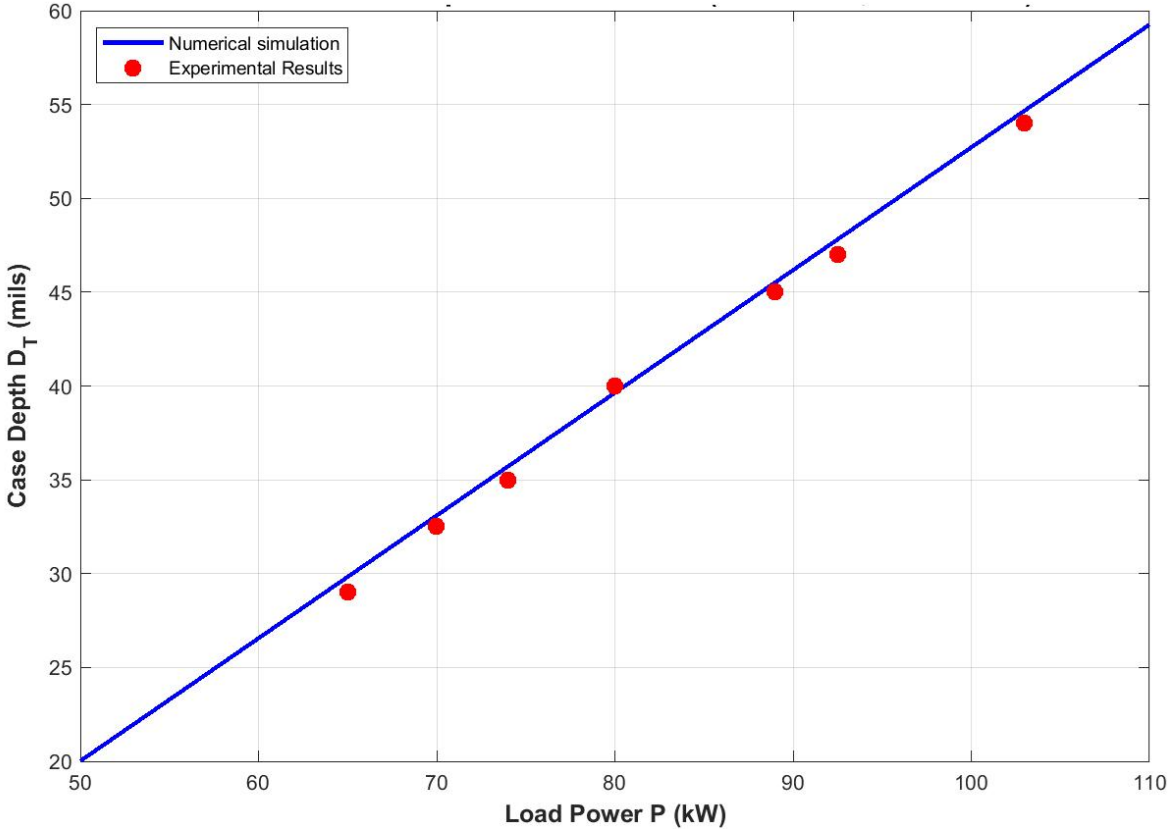

Figure 6. Numerical and experimental results.

4. Conclusion

This comprehensive model for stationary induction hardening provides a complete framework for simulating industrial hardening processes. The key contributions include:

- Complete mathematical formulation of electromagnetic, thermal, and metallurgical physics in 2D axisymmetric coordinates;
- Temperature-dependent material properties for accurate physical predictions;
- Detailed phase transformation kinetics with latent heat effects;
- Comprehensive boundary conditions for convective cooling;
- Numerical implementation guidelines for reproducible simulations;

The model enables prediction and optimization of hardness depth profiles, energy efficiency, and quality control parameters for production. The stationary configuration simplifies the computational approach while maintaining accuracy for practical engineering applications.

Potential enhancements to this model include extension to three-dimensional non-axisymmetric geometries, integration of mechanical stress analysis for distortion predictions, more sophisticated phase transformation models including grain size effects, and coupling with optimization algorithms for automated parameter selection.

Funding: This work received no external funding.

Institutional review board statement: Not applicable.

Informed consent statement: Not applicable.

Data availability statement: The datasets generated during and/or analyzed during the current study are available from the corresponding author on reasonable request.

Conflict of interest: The author declares no conflict of interest.

Abbreviations

Symbol	Definition	Units
A	Magnetic vector potential	T·m (or Wb/m)
A_0	Azimuthal component of magnetic vector potential	T·m
μ	Magnetic permeability	H/m
σ	Electrical conductivity	S/m
ω	Angular frequency	rad/s
f	Frequency	Hz
J	Current density	A/m^2
J_{ext}	External current density in coil	A/m^2
J_0	Azimuthal eddy current density in workpiece	A/m^2
Q_{ind}	Inductive (Joule) heating source	W/m^3
ρ	Density	kg/m^3
C_p	Specific heat capacity	J/(kg·K)
k	Thermal conductivity	W/(m·K)
T	Temperature	°C or K
T_∞	Ambient temperature	°C or K
h	Convective heat transfer coefficient	$W/(m^2 \cdot K)$
ε	Emissivity	–
σ_{SB}	Stefan–Boltzmann constant	$W/(m^2 \cdot K^4)$
Q_{phase}	Latent heat source/sink from phase transformations	W/m^3
X_γ	Austenite phase fraction	–
X_M	Martensite phase fraction	–
A_1	Lower austenitization temperature	°C
A_3	Upper austenitization temperature	°C
t_aus	Austenitization time function	s
M_s	Martensite start temperature	°C
β	Koistinen–Marburger constant	K^{-1}
r	Radial coordinate	m
z	Axial coordinate	m
θ	Azimuthal coordinate	rad
v_z	Axial velocity (zero for stationary case)	m/s
t	Time	s
τ	Heating time	s
∇	Nabla (gradient) operator	1/m
n	Unit normal vector	–

References

1. Dziatkiewicz G, Kuska K, Popiel R. Evolutionary Optimizing Process Parameters in the Induction Hardening of Rack Bar by Response Surface Methodology and Desirability Function Approach under Industrial Conditions. Materials. 2023; 16(17): 5791. doi: 10.3390/ma16175791
2. Garois S, Daoud M, Chinesta F. Data-Driven Inverse Problem for Optimizing the Induction Hardening Process of C45 Spur-Gear. Metals. 2023; 13(5): 997. doi: 10.3390/met13050997
3. Derouiche K, Garois S, Champaney V, et al. Data-Driven Modeling for Multiphysics Parametrized Problems-Application to Induction Hardening Process. Metals. 2021; 11(5): 738. doi: 10.3390/met11050738
4. Dollhofer B, Dietrich S, Schulze V. Improvement of an Electromagnetic-Thermal-Mechanical Coupled Simulation for the Optimization of Complex Processes in Induction Hardening. arXiv preprint. 2024; doi: 10.14940/netsushori.64.ex66
5. Jan J, MacKenzie DS. On the Development of Computational Fluid Dynamics Quenching Simulation Methodology for Effective Thermal Residual Stress Control. Journal of Materials Engineering and Performance. 2024; 33(8): 3986–4010. doi: 10.1007/s11665-023-09106-7
6. Thakur AK, Das B, Chowdhury SG. A data-driven approach to model the martensitic transformation temperature in strain-induced metastable austenitic steels. Materials Today Communications. 2024; 39: 109016. doi: 10.1016/j.mtcomm.2024.109016
7. Sun F, Mino Y, Ogawa T, et al. Evaluation of Austenite–Ferrite Phase Transformation in Carbon Steel Using Bayesian Optimized Cellular Automaton Simulation. Materials. 2023; 16(21): 6922. doi: 10.3390/ma16216922
8. Fisk M, Lindgren L-E, Datchary W, et al. Modelling of induction hardening in low alloy steels. Finite Elements in Analysis and Design. 2018; 144: 61–75. doi: 10.1016/j.finel.2018.03.002
9. Desisa D, Smalcerz A, Kotlan V, et al. Mathematical modelling of thermal stresses of induction surface hardening in axi-symmetric formulation. Surface and Coatings Technology. 2024; 479: 130516. doi: 10.1016/j.surfcoat.2024.130516
10. Li H, Gai K, He L, et al. Non-isothermal phase-transformation kinetics model for evaluating the austenization of 55CrMo steel based on Johnson–Mehl–Avrami equation. Materials & Design. 2016; 92: 731–741. doi: 10.1016/j.matdes.2015.12.110
11. Jamalabadi MYA. Revolutionizing Gear Performance: Cutting-Edge Heat Treatment Methods, Breakthrough Innovations, and Industry Standards for Superior Durability, Journal of Sustainable Engineering Green Technologies. 2025; 1(1): 1–66.
12. Sharifi M, Amani E. Electromagnetic effects on the solidification of a metallic alloy droplet impacting onto a surface. Colloids and Surfaces A: Physicochemical and Engineering Aspects. 2024; 700: 134806. doi: 10.1016/j.colsurfa.2024.134806
13. Amani E, Sharifi M. Metallic alloy droplet impact and solidification under an alternating magnetic field: Scaling laws and regime maps. International Journal of Thermal Sciences. 2025; 210: 109645. doi: 10.1016/j.ijthermalsci.2024.109645
14. Sharifi M. Investigating the influence of magnetic field on heat transfer in turbulent ferromagnetic fluid over a backward-facing step. Physics of Fluids. 2024; 36(12): 125152. doi: 10.1063/5.0244293
15. Rudnev V, Loveless D, Cook RL. Handbook of Induction Heating, 2nd ed. CRC Press; 2017. doi: 10.1201/9781315117485
16. Hömberg D. A mathematical model for induction hardening including mechanical effects. Nonlinear Analysis: Real World Applications. 2004; 5(1): 55–90. doi: 10.1016/S1468-1218(03)00017-8
17. Mühlbauer A. History of Induction Heating and Melting. Vulkan-Verlag GmbH; 2008.
18. Coupard D, Palin-luc T, Bristiel P, et al. Residual stresses in surface induction hardening of steels: Comparison between experiment and simulation. Materials Science and Engineering: A. 2008; 487(1–2): 328–339. doi: 10.1016/j.msea.2007.10.047
19. Hirao M, Ogi H. Electromagnetic Acoustic Transducers: Noncontacting Ultrasonic Measurements using EMATs. Springer; 2017. doi: 10.1007/978-4-431-56036-4
20. Bhadeshia HKDH, Honeycombe RWK. Steels: Microstructure and Properties. Elsevier; 2017.
21. Koistinen DP, Marburger RE. A general equation prescribing the extent of the austenite-martensite transformation in pure iron-carbon alloys and plain carbon steels. Acta Metallurgica. 1959; 7(1): 59–60. doi: 10.1016/

0001-6160(59)90170-1
22. Pinheiro PM, Junio JU, Gonçalves LAP, et al. Modeling and Simulation of the Induction Hardening Process: Evaluation of Gear Deformations and Parameter Optimization. Processes. 2024; 12(7): 1428. doi: 10.3390/pr12071428
23. Toros S, Altinel K. Contribution of functionally graded material modelling on finite element simulation of rod end parts in automotive steering system. Journal of Mechanical Science and Technology. 2016; 30(7): 3137–3141. doi: 10.1007/s12206-016-0623-6
24. Sjöström S. Interactions and constitutive models for calculating quench stresses in steel. Materials Science and Technology. 1985; 1(10): 823–829. doi: 10.1179/mst.1985.1.10.823
25. Kabir H, Aghdam MM. A generalized 2D Bézier-based solution for stress analysis of notched epoxy resin plates reinforced with graphene nanoplatelets. Thin-Walled Structures. 2021; 169: 108484. doi: 10.1016/j.tws.2021.108484
26. Wang Y, Gu Y, Liu J. A domain-decomposition generalized finite difference method for stress analysis in three-dimensional composite materials. Applied Mathematics Letters. 2020; 104: 106226. doi: 10.1016/j.aml.2020.106226
27. Jamalabadi MYA. An Improvement of Port-Hamiltonian Model of Fluid Sloshing Coupled by Structure Motion. Water. 2018a; 10(12): 1721. doi: 10.3390/w10121721
28. Induction Systems, Inc. Operator Instruction Manual Version 9. ProScan; n.d.

Appendix A. Material properties

The material properties of AISI 4140 steel used in the simulation are presented in **Appendix A**. The isothermal hardening behavior under varying strain rates is illustrated in **Figures A1–A3**, which depict 3D contour plots of flow stress as a function of temperature and plastic strain at strain rates of 0.001 s^{-1}, 0.01 s^{-1}, and 0.1 s^{-1}, respectively, capturing the material's thermomechanical response under quasi-static to moderate dynamic conditions. **Figures A4** and **A5** plot the 2D version of T25 °C isothermal hardening at strain rate 0.001 s^{-1} and 1000 s^{-1}.

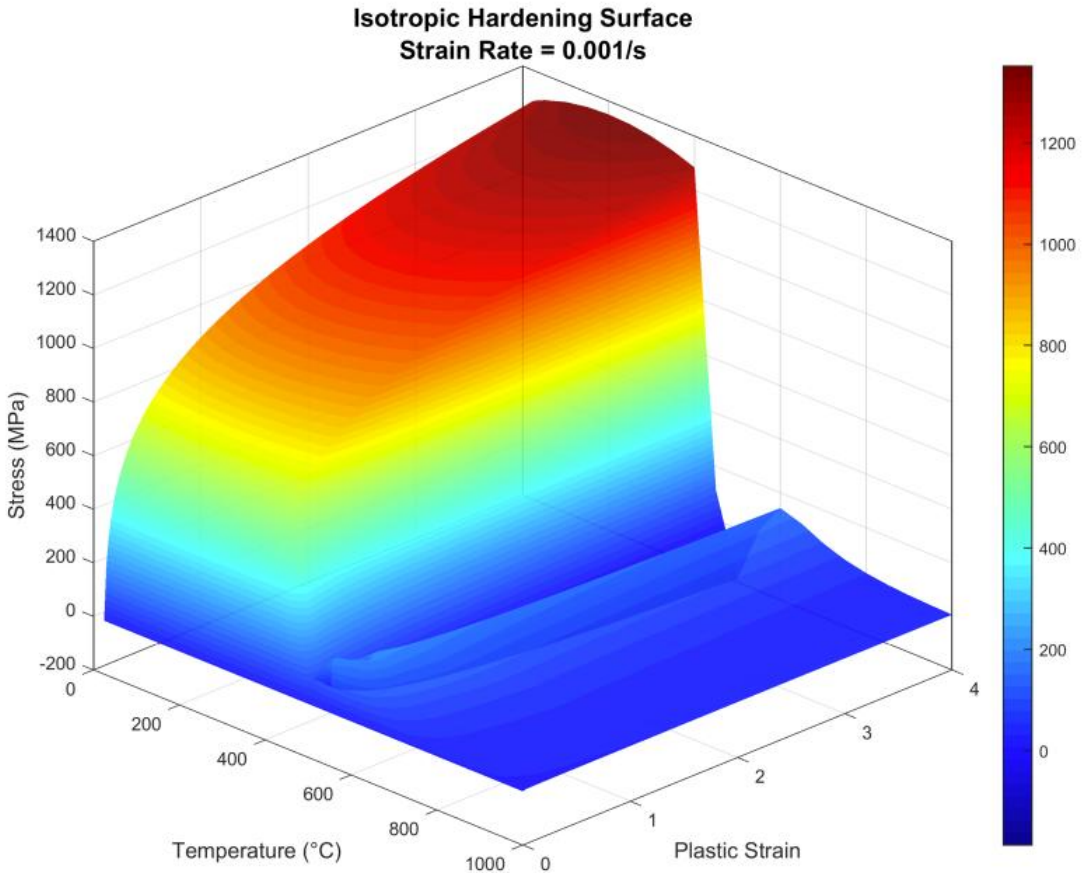

Figure A1. 3D isothermal hardening at strain rate 0.001 s^{-1}.

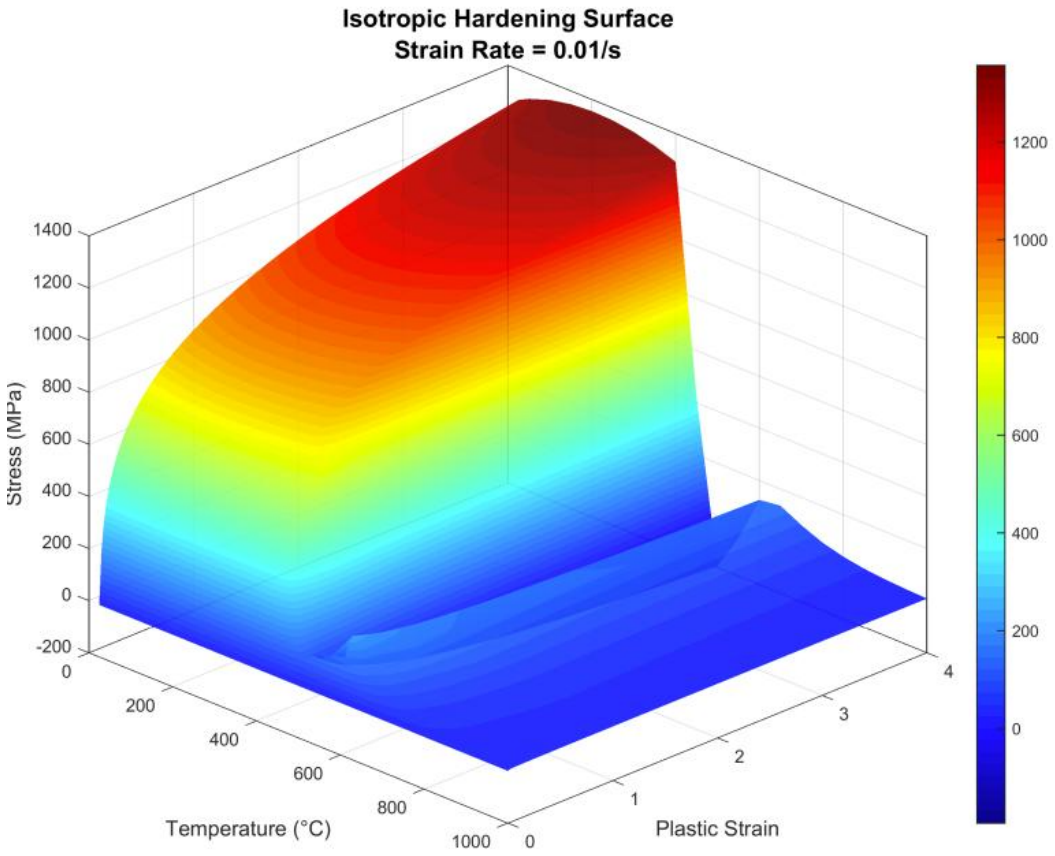

Figure A2. 3D isothermal hardening at strain rate 0.01 s^{-1}.

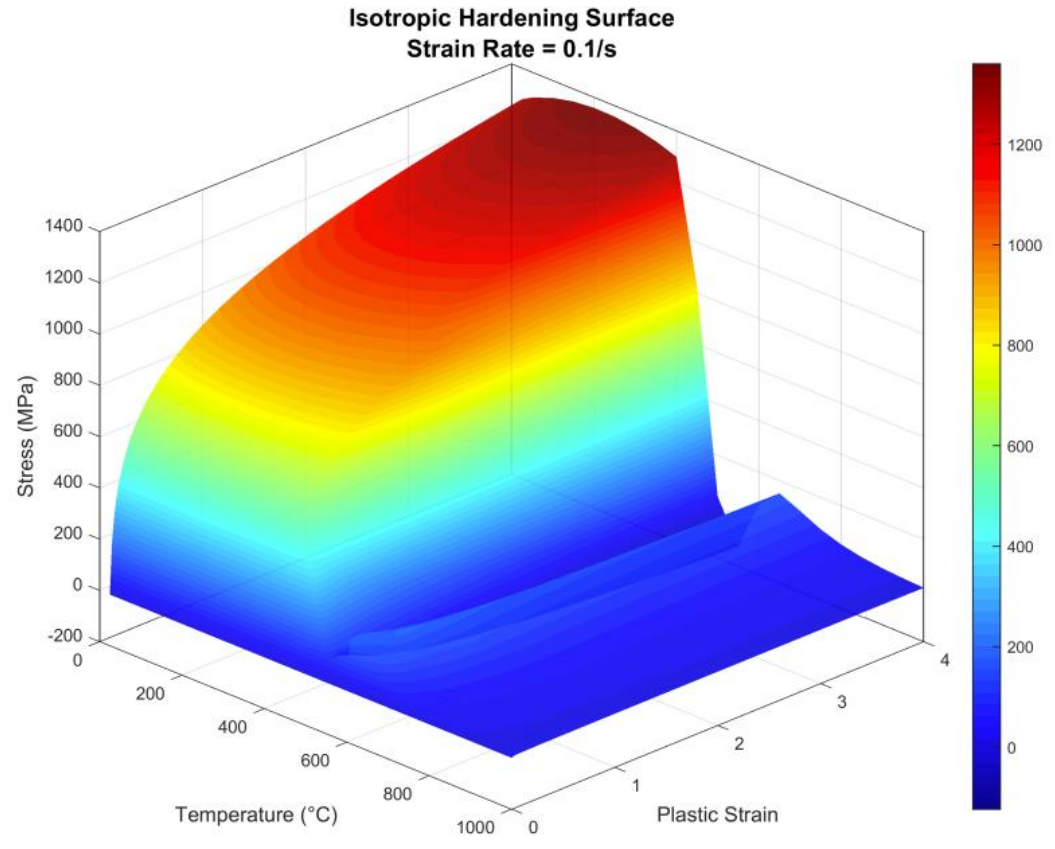

Figure A3. 3D isothermal hardening at strain rate 0.1 s^{-1}.

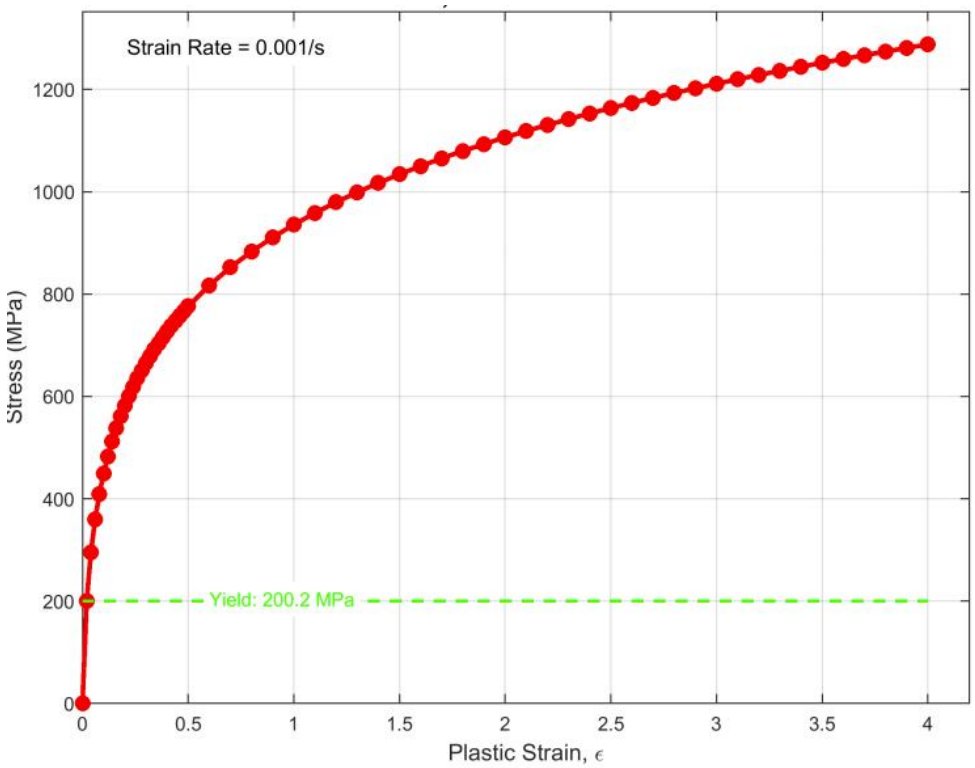

Figure A4. T25 °C isothermal hardening at strain rate 0.001 s^{-1}.

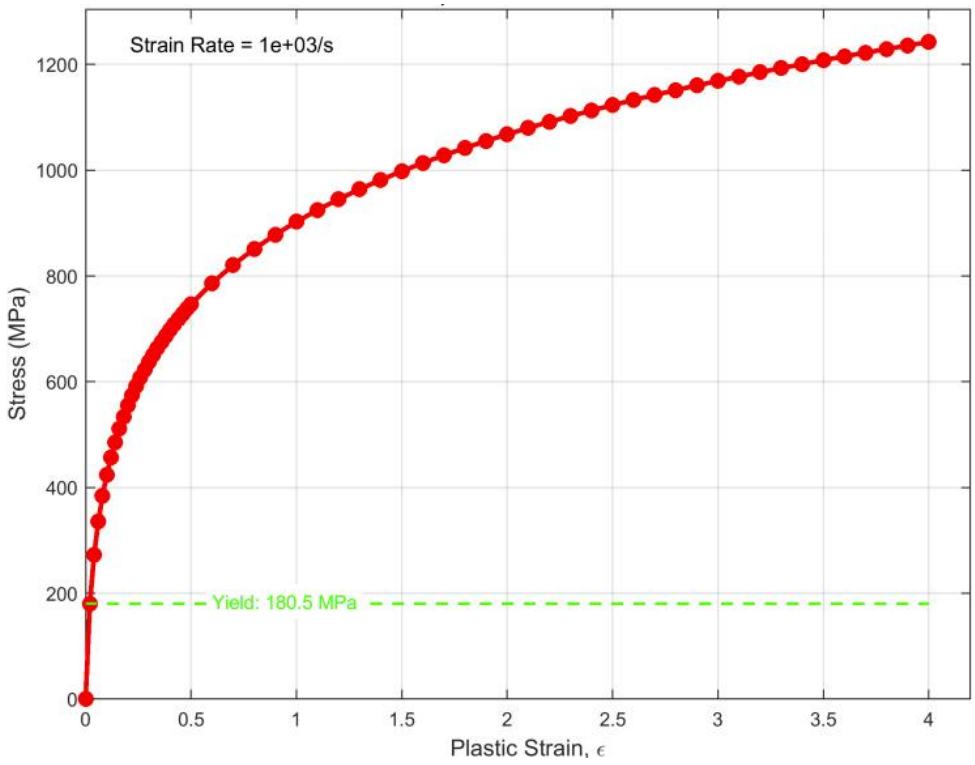

Figure A5. T25 °C isothermal hardening at strain rate 1000 s^{-1}.

Temperature-dependent elastic and thermal properties are shown in subsequent figures: bulk modulus (**Figure A6**), density (**Figure A7**), electrical conductivity (**Figure A8**), thermal expansion coefficient (**Figure A9**), Poisson's ratio (**Figure A10**), shear modulus (**Figure A11**), specific heat capacity (**Figure A12**), thermal conductivity (**Figure A13**), and Young's modulus (**Figure A14**), all of which are critical for accurately modeling the coupled electromagnetic-thermal-metallurgical behavior during induction hardening. Additionally, the strain rate sensitivity at

room temperature is presented in **Figure A15**, while **Figure A16** shows the thermal softening trend at a constant strain rate of 0.001 s^{-1}.

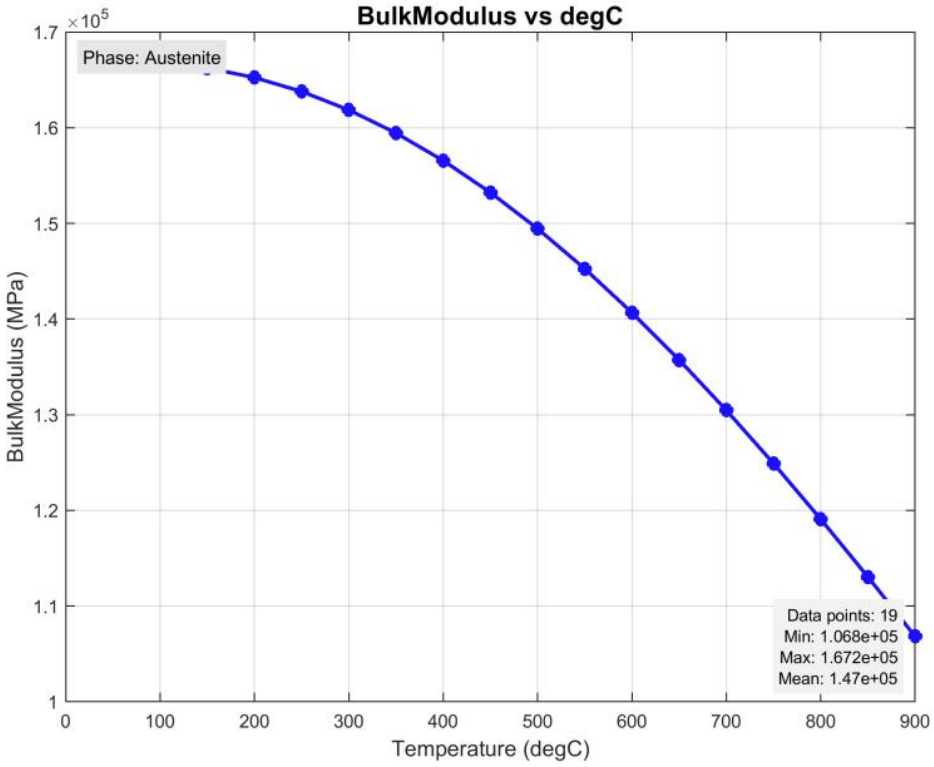

Figure A6. Bulk Modulus.

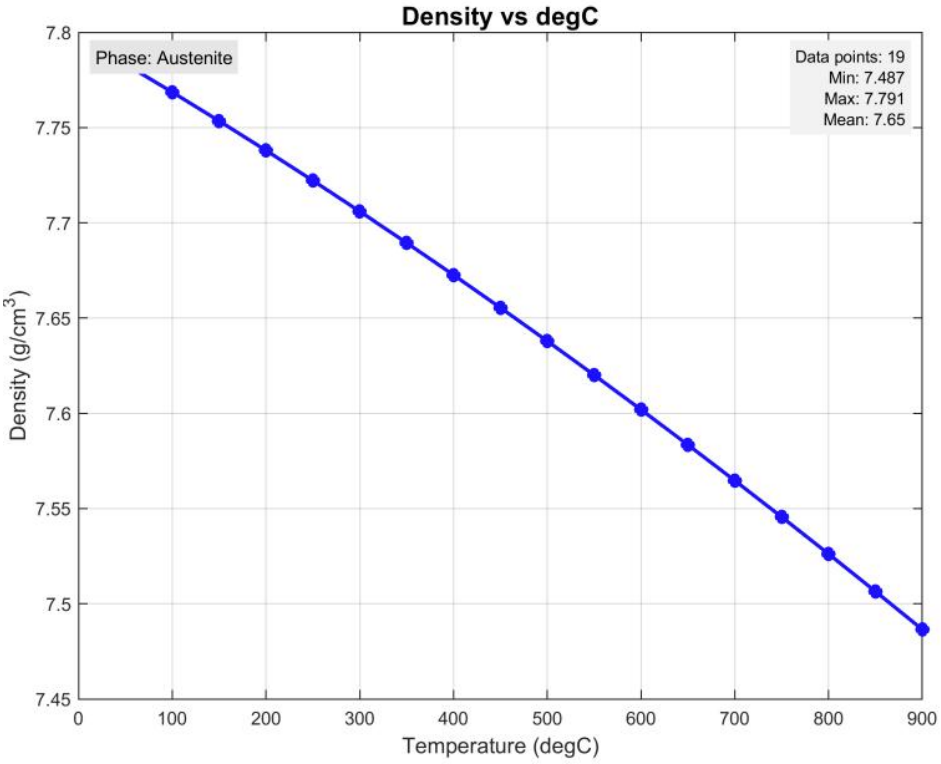

Figure A7. Density.

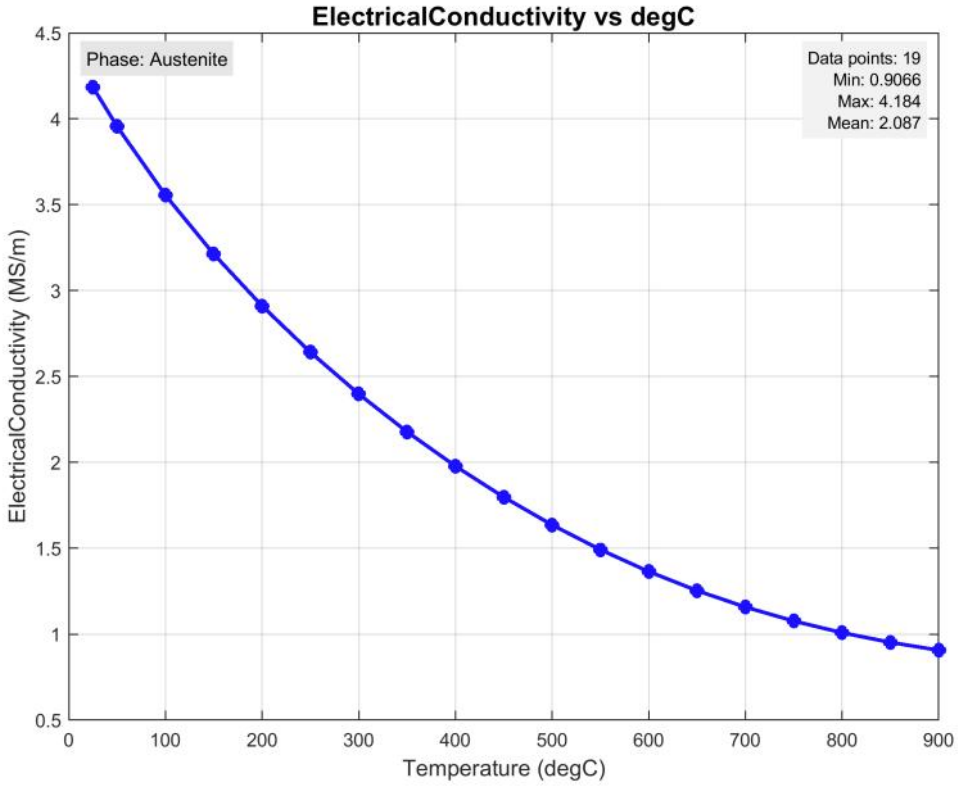

Figure A8. Electrical Conductivity.

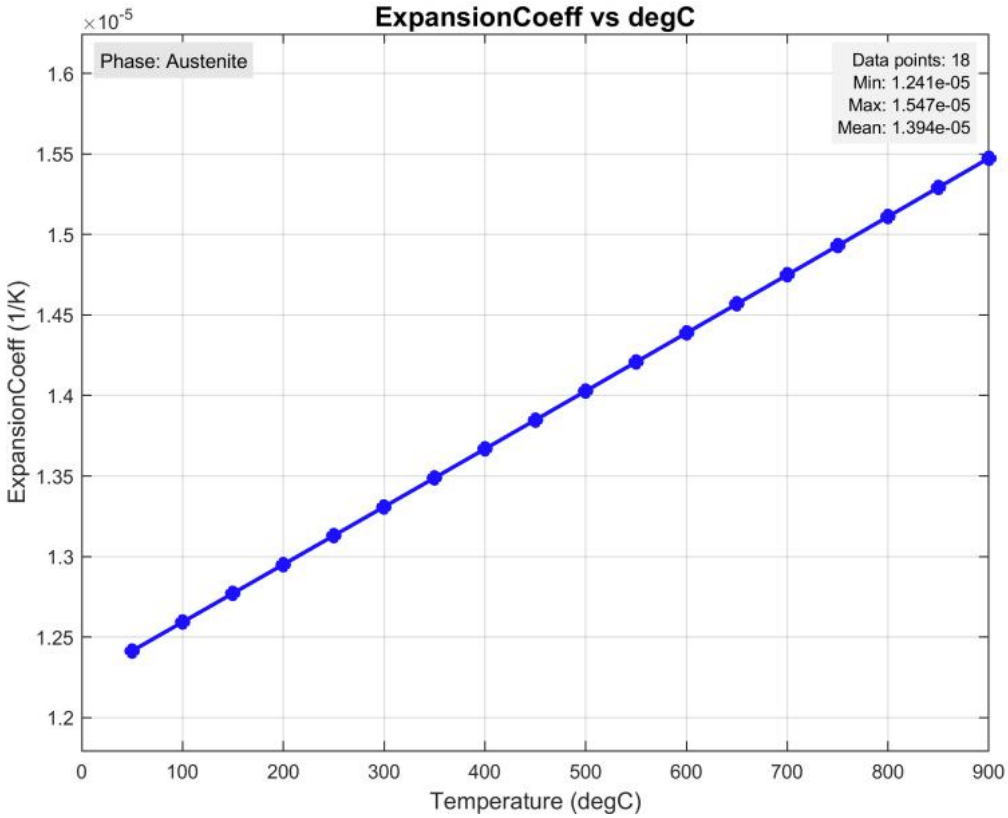

Figure A9. Expansion Coefficient.

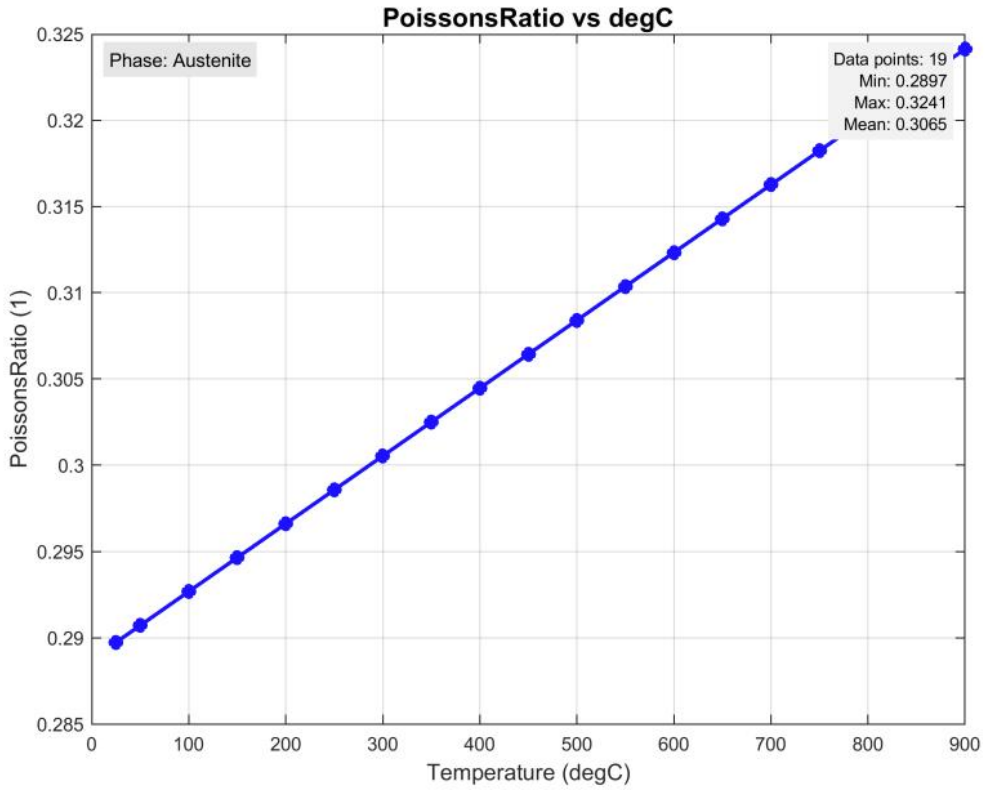

Figure A10. Poisson's Ratio.

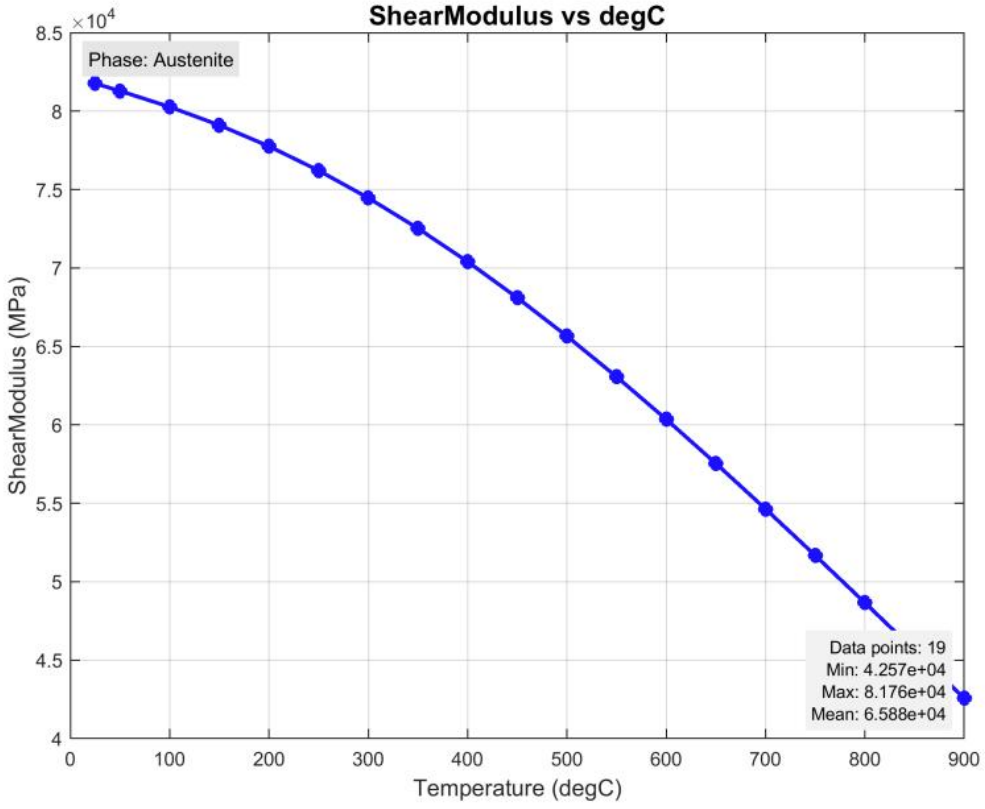

Figure A11. Shear Modulus.

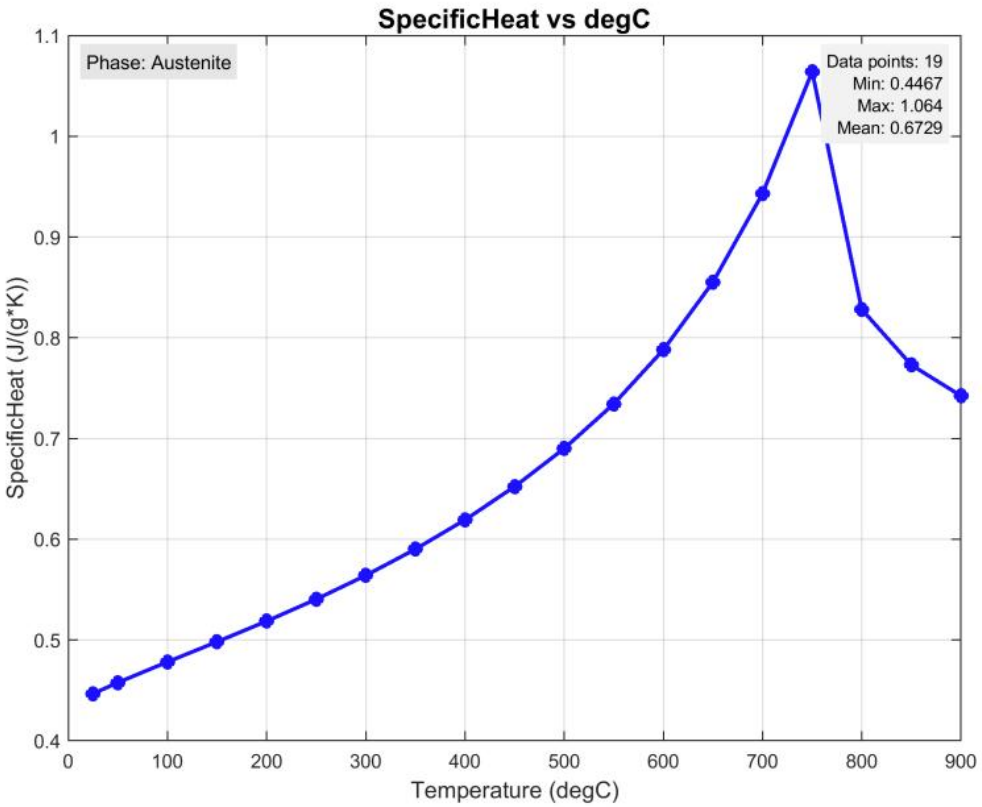

Figure A12. Specific Heat.

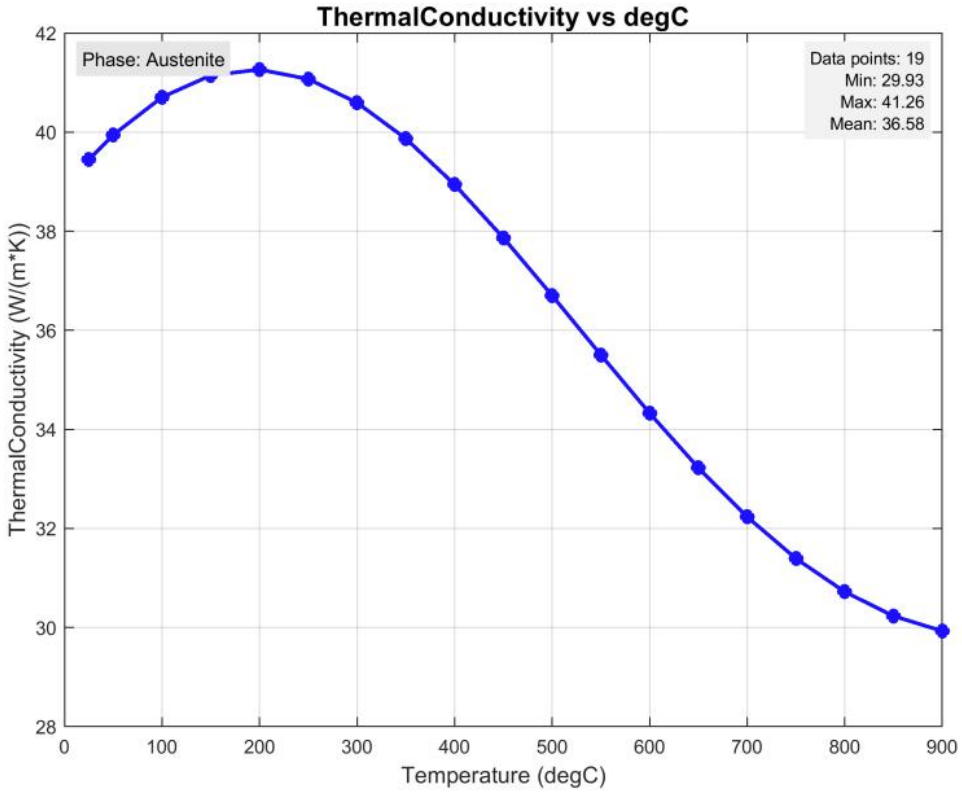

Figure A13. Thermal Conductivity.

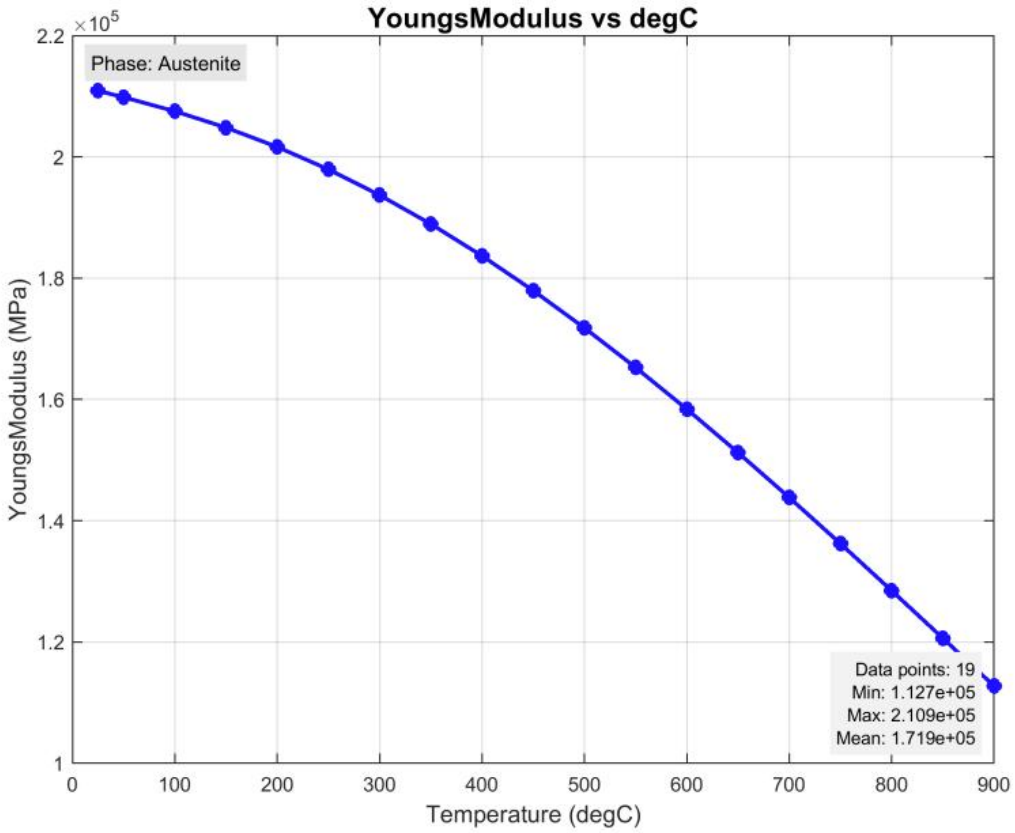

Figure A14. Young's Modulus.

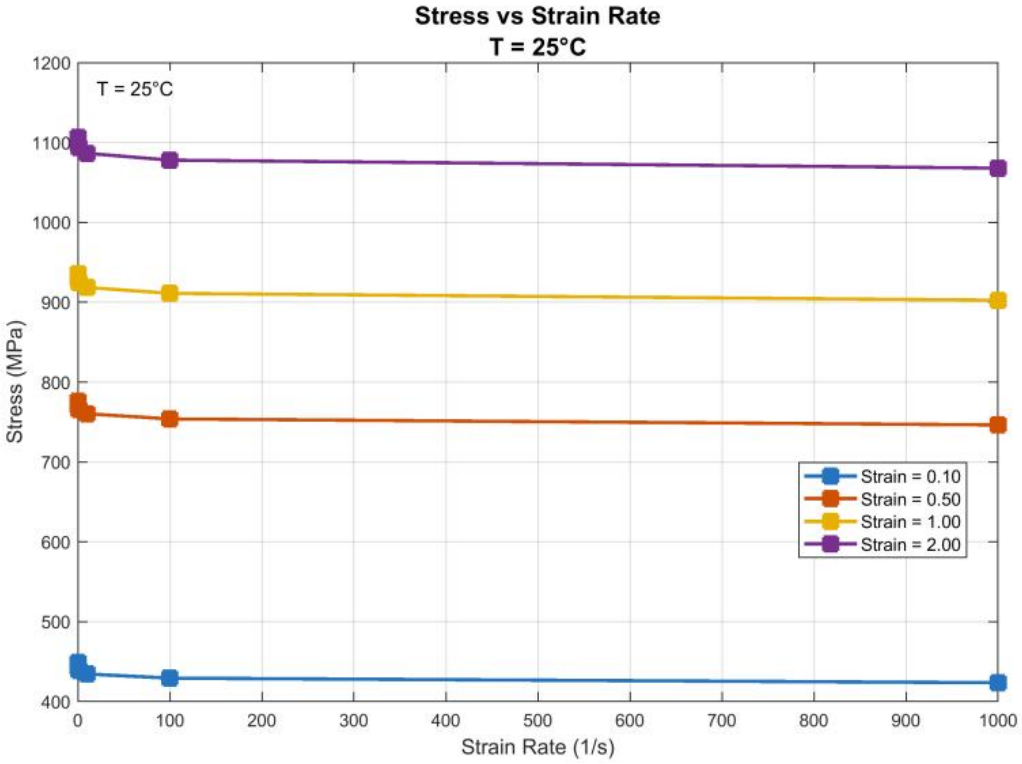

Figure A15. Stress vs Strain Rate at T25 °C.

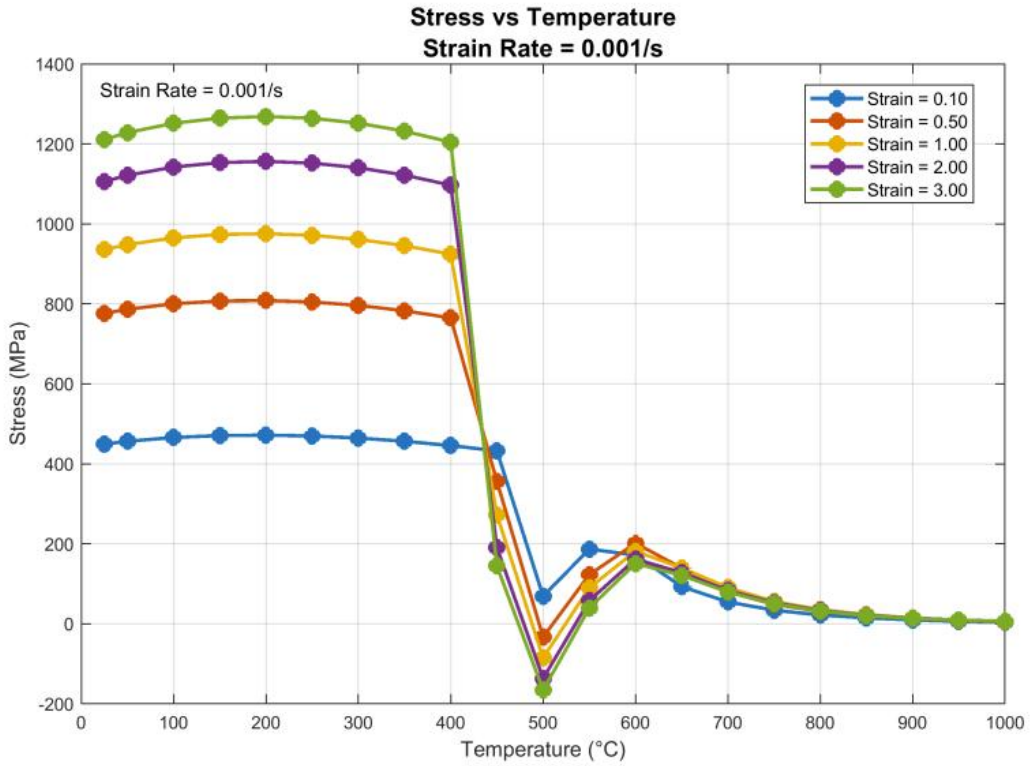

Figure A16. Stress vs Temperature at Strain Rate 0.001.

TTT (Time-Temperature-Transformation) data comes from:

- Total temperature points: 45 (ferrite), 41 (pearlite), 25 (bainite)
- Transformation fractions tracked: 26 levels (0.1% to 99%)
- Total data points: Over 2900 time-temperature-fraction triplets
- Temperature range: 340–780 °C (covering all transformation regimes)
- Time range: 0.1 s to 10^8 s (over 3 years!)

This comprehensive dataset enables accurate prediction of phase transformations for any thermal history.

Figures A17–A19 show TTT (Time-Temperature-Transformation) diagrams which visualize the phase transformation kinetics used in the induction hardening simulation. **Figure A17** presents the TTT diagram used to model phase transformation kinetics during cooling. The diagram displays C-curves for diffusive transformations: austenite to ferrite (blue), pearlite (green), and bainite (orange). Horizontal red lines indicate martensite start (M_s) and completion temperatures. The diagram covers a temperature range of 340–780 °C and times from 0.1 s to 10^8 s, providing a comprehensive dataset for predicting phase evolution under varying thermal histories.

Figure A18 illustrates the same TTT diagram as **Figure A17,** overlaid with four characteristic cooling curves corresponding to different quenching methods: water quench (∼1000 °C/s, green), oil quench (∼100 °C/s, blue), air cooling (∼10 °C/s, purple), and furnace cooling (∼1 °C/s, brown). The paths demonstrate how cooling rate determines the resulting microstructure—bypassing diffusive transformations for martensite formation or intersecting C-curves for ferrite, pearlite, or bainite.

Figure A19 provides a detailed view of the lower temperature range (approximately 250–600 °C) of the TTT diagram, emphasizing bainite transformation kinetics and martensite formation. The bainite C-curve (orange) and martensite lines are highlighted, along with cooling paths typical of induction hardening. This zoomed-in representation aids in visualizing the critical cooling rates required to avoid bainite and achieve fully martensitic microstructures in the hardened case.

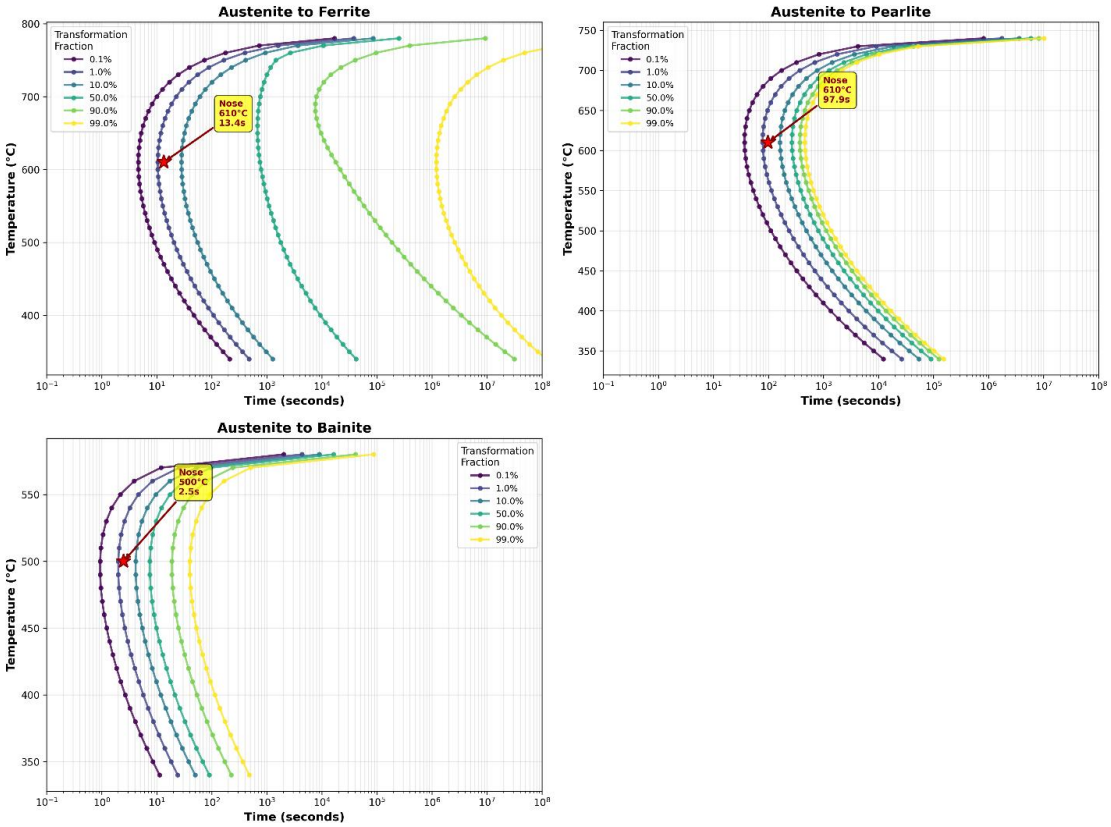

Figure A17. Time–Temperature–Transformation (TTT) diagram for AISI 4140 steel.

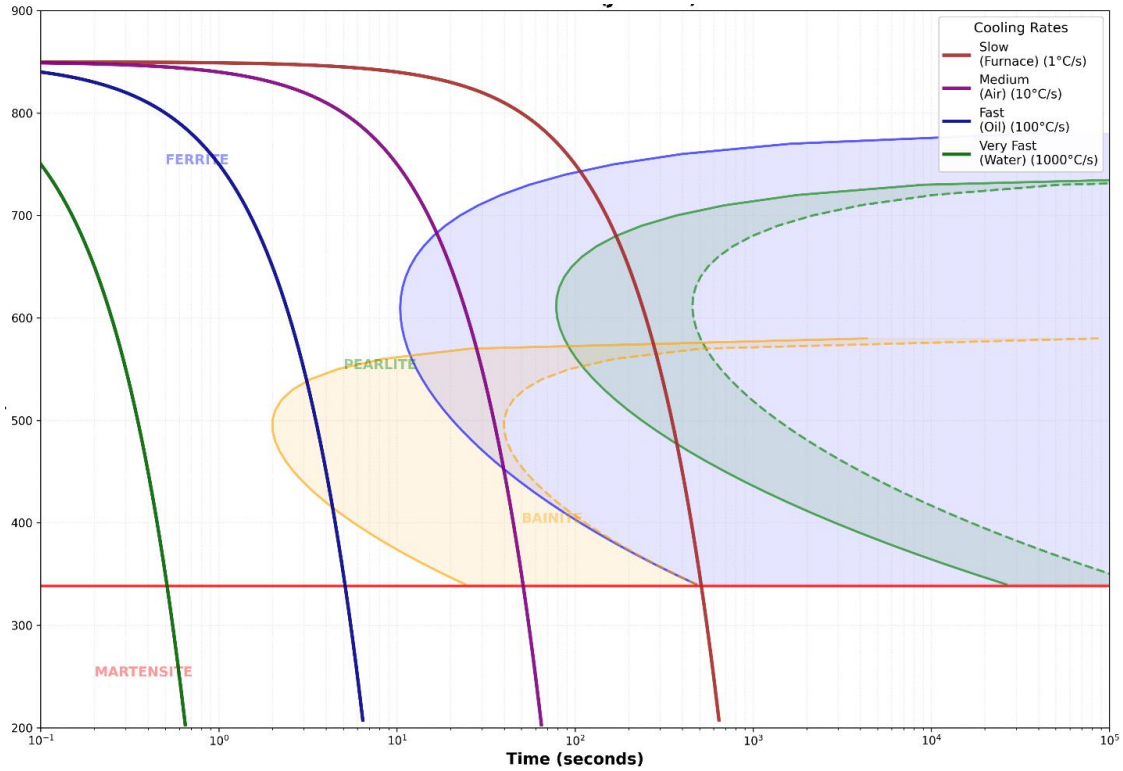

Figure A18. TTT diagram with example cooling paths for different quenching methods.

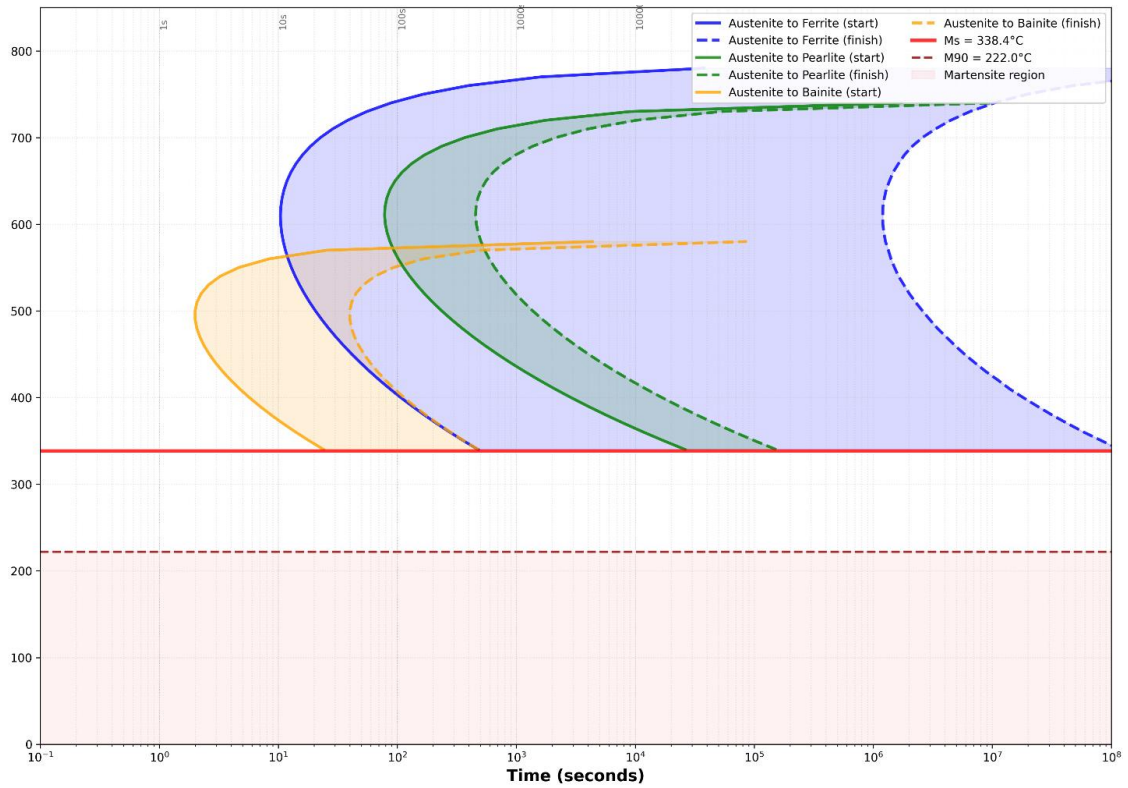

Figure A19. Enlarged view of the low-temperature region of the TTT diagram focusing on bainite and martensite formation.

In **Figures A17–A19**

1. **Austenite to ferrite (blue curves)**
   - Temperature range: 340 °C to 780 °C
   - Nose temperature: ~610 °C at 13.4 s
   - Characteristics: Forms at higher temperatures during slow cooling
   - Phase region: Blue shaded area
2. **Austenite to pearlite (green curves)**
   - Temperature range: 340 °C to 740 °C
   - Nose temperature: ~610 °C at 98.0 s
   - Characteristics: Forms at intermediate temperatures
   - Phase region: Green shaded area
3. **Austenite to bainite (orange curves)**
   - Temperature range: 340 °C to 580 °C
   - Nose temperature: ~500 °C at 2.5 s
   - Characteristics: Forms at lower temperatures, faster than ferrite/pearlite
   - Phase region: Orange shaded area
4. **Martensite (red horizontal lines)**
   - Ms (Martensite start): 338.4 °C, M_{50}: 303.4 °C, M_{90}: 222.0 °C
   - Characteristics:
     - Displacive (diffusionless) transformation
     - Time-independent - depends only on temperature
     - Forms when cooled below Ms faster than the nose curves

- Phase region: Below the red line

Each transformation has a characteristic C-curve shape with a "nose" —the point of fastest transformation—Left of the nose: Slower transformation (lower undercooling)—At the nose: Fastest transformation rate—Right of the nose: Slower transformation (carbon diffusion becomes limiting). In **Figure A18**, the diagram shows example cooling curves:

1. **Very Fast (water quench—1000 °C/s)—green line**
   - Bypasses all diffusive transformations
   - Goes straight through to the martensite region
   - Result: ~100% martensite (hard and brittle)
2. **Fast (oil quench—100 °C/s)—blue line**
   - Bypasses ferrite and pearlite
   - May catch the upper bainite region
   - Finishes as martensite
   - Result: Martensite + possible small bainite (very hard)
3. **Medium (air cool—10 °C/s) —purple line**
   - Intersects pearlite nose
   - Some bainite formation
   - Result: Mixed pearlite + bainite + martensite
4. **Slow (furnace cool—1 °C/s)—brown line**
   - Intersects both ferrite and pearlite noses
   - Full transformation at high temperatures
   - Result: Ferrite + pearlite (soft and ductile)

From the diagrams, we can determine the Critical Cooling Rate (minimum cooling rate to achieve 100% martensite):

- Must cool fast enough to avoid the bainite nose (~500 °C, 2.5 s)
- Estimated critical cooling rate: ~200–500 °C/s
- Water quenching (1000 °C/s) easily exceeds this
- Oil quenching (100 °C/s) is marginal - may get some bainite

Application to Induction Hardening on the Surface of the Pin shows:

- Heating: Rapid induction heating to ~850–900 °C → 100% austenite
- Cooling: Water quench at ~1000 °C/s or higher
- Path on TTT: Shoots straight down, missing all noses
- Final structure: ~100% martensite (hard, wear-resistant)

Mid-Depth:

- Heating: Slower temperature rise, reaches ~700–750 °C → Partial austenite
- Cooling: Moderate cooling rate ~100–200 °C/s
- Path on TTT: May graze bainite nose
- Final structure: Martensite + some bainite + retained austenite

Core:

- Heating: Minimal heating, stays below A_1 (723 °C)
- Cooling: Slow cooling
- Path on TTT: Never transforms to austenite
- Final structure: Original ferrite + pearlite (tough, ductile)

Quantitative Transformation Data are summarized in **Tables A1** and **A2**. **Table A1** shows that bainite forms much faster than ferrite or pearlite at the same temperature.

Table A1. Transformation times at 500 ℃.

Phase	1% Transform	50% Transform	99% Transform
Ferrite	9.1 s	157 s	260,000 s
Pearlite	7.7 s	94 s	189,000 s
Bainite	2.7 s	13 s	8220 s

Table A2. Transformation times at 600 ℃.

Phase	1% Transform	50% Transform	99% Transform
Ferrite	4.6 s	101 s	36,000 s
Pearlite	3.9 s	62 s	24,000 s
Bainite	Not stable	Not stable	Not stable

Note: At 600 °C, bainite doesn't form (outside its temperature range).

Practical implications from **Figures A17–A19** for heat treatment design are:

1. To get martensite: Cool faster than ~200 °C/s from austenitization temperature
2. To get bainite: Cool at 10–100 °C/s and hold at 400–500 °C
3. To get pearlite: Cool at 1–10 °C/s
4. To get ferrite: Very slow cool (<1 °C/s) or anneal

For Induction Hardening:

- Case depth control: Controlled by heating depth (electromagnetic skin depth)
- Hardness gradient: Automatic from cooling rate gradient
- Tempering: May be needed to reduce the brittleness of martensite
- Residual stress: Martensite expansion creates beneficial compressive stress

Figure A20 shows the flowchart of this process. The Multiphysics simulation models the induction hardening of a cylindrical steel pin by tracking the evolution of five phases—austenite, ferrite, pearlite, bainite, and martensite—using phase transformation kinetics containing TTT curves, Ms temperatures, and thermomechanical properties. The process initiates with electromagnetic heating (120 kHz) that austenitizes the surface above A_1 temperature, followed by water quenching where the cooling rate dictates the final microstructure: rapid surface cooling bypasses diffusive transformations to form martensite via the Koistinen-Marburger equation, moderate mid-depth cooling permits partial bainite formation before martensitic transformation, and slow core cooling reverts to ferrite and pearlite described by JMAK kinetics, while the model fully couples latent heat release, transformation-induced plasticity, and volumetric strains to predict residual stresses and the final hardness gradient.

Appendix B. Heat transfer mechanism

Also, the heat transfer of radiation is h = 150 W/m^2 at the maximum temperature of 1100, which is also included in the calculation. The provided data in **Figure A21** illustrate the relationship between planetary surface temperature and both convective and radiative heat fluxes. As surface temperature increases from 0 °C to 300 °C, convective heat flux rises moderately from 3.5 × 10^4 W/m^2 to a peak of approximately 4.0 × 10^4 W/m^2, while radiative flux increases steadily from 10 to 25 W/m^2. Beyond 300 °C, convective flux declines sharply, falling to 0.1 × 10^4 W/m^2 by 1000 °C, indicating a transition where radiative cooling becomes increasingly dominant. Radiative flux continues to grow, reaching 80 W/m^2 at 1000 °C, demonstrating that at high temperatures, radiation becomes the primary heat loss mechanism despite the drop

in convective transfer, likely due to atmospheric or physical constraints on convection efficiency.

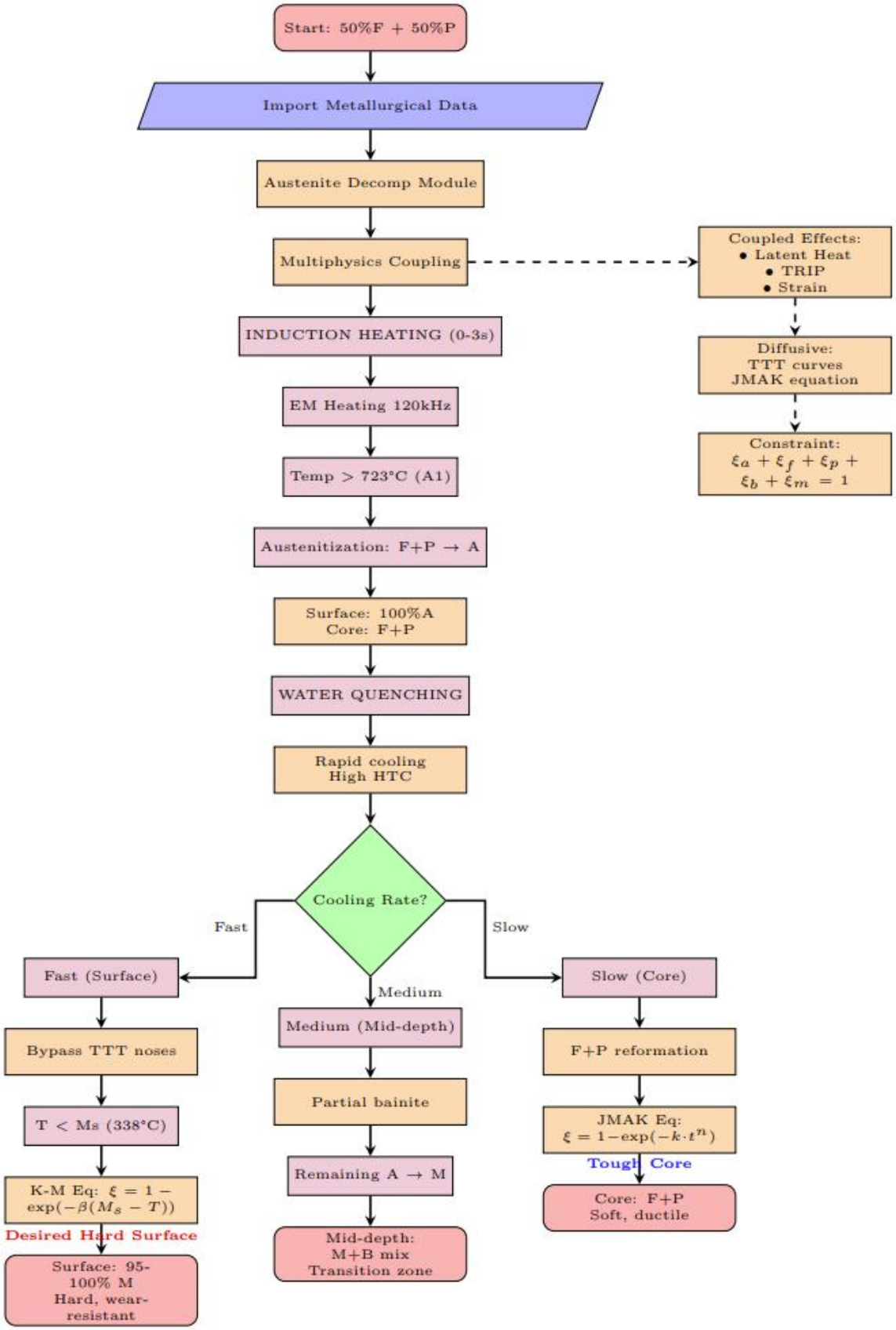

Figure A20. Flowchart of heat treatment design.

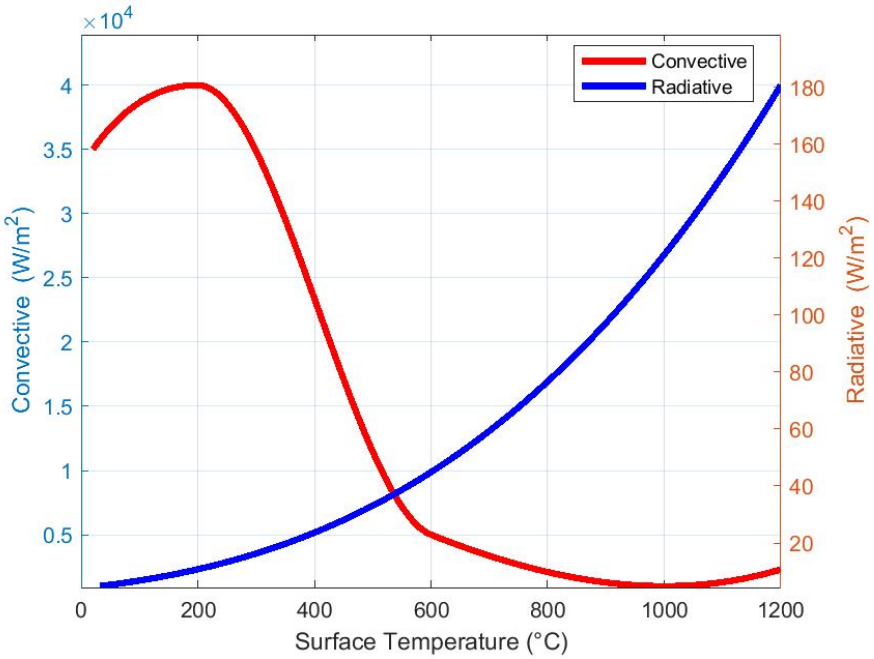

Figure A21. Forced convection of water spray vs radiative heat transfer.

Appendix C. Stress calculation

In the current paper, the stress is calculated by solving the momentum balance equation for a deformable solid under mechanical, thermal, and phase transformation effects. Specifically, the developed code solves the following governing equation in the Quasi-static formulation:

$$\nabla \cdot \sigma + F_v = 0 \tag{A1}$$

where:

σ is the Cauchy stress tensor,

F_v is the body force per unit volume. Hereby, the Quasi-static assumption inertial terms are neglected.

As well as the constitutive relation (stress–strain law), the total strain is decomposed into several contributions:

$$\varepsilon_{total} = \varepsilon_{el} + \varepsilon_{th} + \varepsilon_{pl} + \varepsilon_{tr} \tag{A2}$$

where:

ε_{el} = elastic strain,

ε_{th} = thermal strain,

ε_{pl} = plastic strain (if plasticity is active),

ε_{tr} = transformation strain (due to phase change).

The elastic stress is then given by Hooke's law (linear elasticity):

$$\sigma = C : \varepsilon_{el} \tag{A3}$$

with C being the fourth-order stiffness tensor (depending on Young's modulus and Poisson's ratio). Furthermore, the plasticity model is isotropic hardening with a hardening function. Phase-transformation strains are coupled from the phase calculation, and thermal strains are included because temperature is solved by the heat transfer physics and passed to solid mechanics. The model plots Von Mises equivalent stress (a scalar measure of stress intensity), where is a function of the deviatoric stress tensor.